

M3S-Net: Multimodal Feature Fusion Network Based on Multi-scale Data for Ultra-short-term PV Power Forecasting

Penghui Niu^a, Taotao Cai^b, Suqi Zhang^{c,*}, Junhua Gu^{a,d,*}, Ping Zhang^{a,d}, Qiqi Liu^e and Jianxin Li^f

^aSchool of Artificial Intelligence, Hebei University of Technology, Tianjin 300401, China

^bUniversity of Southern Queensland, Toowoomba 487-535, Australia

^cSchool of Information Engineering, Tianjin University of Commerce, Tianjin 300134, China

^dHebei Province Key Laboratory of Big Data Calculation, Hebei University of Technology, Tianjin 300401, China

^eTrustworthy and General AI Lab, School of Engineering, Westlake University, Hangzhou, 310030, China

^fDiscipline of Business Systems and Operations, School of Business and Law, Edith Cowan University, Joondalup, WA 6027, Australia

ARTICLE INFO

Keywords:

Ultra-short-term PV power forecasting
Multimodal feature fusion
Ground-based cloud image
Mamba architecture
Cross-modal interaction

ABSTRACT

The inherent intermittency and high-frequency variability of solar irradiance, particularly during rapid cloud advection, present significant stability challenges to high-penetration photovoltaic (PV) grids. Although multimodal forecasting has emerged as a viable mitigation strategy, existing architectures predominantly rely on shallow feature concatenation and binary cloud segmentation, thereby failing to capture the fine-grained optical features of clouds and the complex spatiotemporal coupling between visual and meteorological modalities. To bridge this gap, this paper proposes M3S-Net, a novel multimodal feature fusion network based on multi-scale data for ultra-short-term PV power forecasting. First, a multi-scale partial channel selection network leverages partial convolutions to explicitly isolate the boundary features of optically thin clouds, effectively transcending the precision limitations of coarse-grained binary masking. Second, a multi-scale sequence to image analysis network employs Fast Fourier Transform (FFT)-based time-frequency representation to disentangle the complex periodicity of meteorological data across varying time horizons. Crucially, the model incorporates a cross-modal Mamba interaction module featuring a novel dynamic “C-matrix swapping” mechanism. By exchanging state-space parameters between visual and temporal streams, this design conditions the state evolution of one modality on the context of the other, enabling deep structural coupling with linear computational complexity, thus overcoming the limitations of shallow concatenation. Experimental validation on the newly constructed fine-grained PV power dataset (FGPD) demonstrates that M3S-Net achieves a mean absolute error (MAE) reduction of 6.2% and a R-squared (R^2) of 0.964 in 10-minute forecasts compared to state-of-the-art (SOTA) baselines. These results confirm that deep cross-modal interaction and micro-physical cloud modeling are instrumental in mitigating ramp-rate risks in real-time grid operations. The dataset and source code will be available at <https://github.com/she1110/FGPD>.

1. Introduction

The global transition toward carbon-neutral energy paradigms has precipitated an exponential expansion in solar photovoltaic capacity. While this proliferation is underpinned by the inherent modularity and precipitous decline in the levelized cost of energy of PV technologies, their large-scale integration introduces profound stochasticity into modern power grids [1]. Unlike dispatchable fossil-fuel generation, PV output is intrinsically coupled with atmospheric dynamics, exhibiting volatility across spatiotemporal scales ranging from seasonal cycles to sub-second fluctuations [2]. As PV penetration rates approach critical thresholds within national grids, the stability of the power system becomes increasingly susceptible to this variability [3]. Consequently, the operational imperative has shifted from merely predicting diurnal cycles to mitigating “ramp events,” which are the rapid, high-magnitude power gradients primarily induced by cloud advection [4]. In this context, ultra-short-term

forecasting (with horizons spanning minutes to one hour) transcends its traditional role as an ancillary service, emerging as a foundational prerequisite for real-time economic dispatch, frequency regulation, and the efficient operation of ancillary service markets [5].

Conventional forecasting frameworks rely predominantly on numerical weather prediction (NWP) models or statistical persistence methods. While NWP models provide essential synoptic-scale context for day-ahead planning, their inherent spatiotemporal resolution limitations (typically kilometers and hours) and high latency render them insufficient for capturing the localized, high-frequency transients characteristic of ultra-short-term horizons. Similarly, statistical approaches predicated solely on historical autocorrelation, such as autoregressive integrated moving average or early recurrent neural networks (RNNs), establish a baseline but lack the capacity to anticipate exogenous meteorological disturbances, effectively operating in a purely reactive modality [6, 7, 8]. These models often fail to capture the abrupt phase shifts caused by rapid cloud movement, leading to significant prediction errors during ramp events.

*Corresponding author

✉ qingxinqazxsw@163.com (P. Niu); taotao.cai@unisoq.edu.au (T. Cai);
suqizhang@tjcu.edu.cn (S. Zhang); jhguhebut@163.com (J. Gu);
zhangping@hebut.edu.cn (P. Zhang); qiqi6770304@gmail.com (Q. Liu);
jianxin.li@ecu.edu.au (J. Li)

To overcome these limitations, recent scholarships have pivoted toward deep learning architectures capable of ingesting high-dimensional data. Single-modal approaches utilizing historical power data, such as bi-directional gated recurrent units (Bi-GRU), have demonstrated that capturing temporal dependencies in both forward and reverse directions can significantly reduce mean squared error (MSE) compared to standard ensembles [9]. Concurrently, the integration of ground-based cloud images (GCI) has established a parallel research trajectory focused on visual irradiance mapping. Early works explicitly modeled cloud kinematics via optical flow, effectively bifurcating the SOTA into two distinct domains: temporal sequence modeling and computer vision-based GCI analysis [10].

Despite the sophistication of these individual approaches, a critical research gap persists: the inability of existing models to effectively synthesize the complex, multi-scale dynamics of PV generation when influenced jointly by meteorological trends and chaotic cloud dynamics. First, while GCI offers a theoretical solution to the latency inherent in time-series data, current implementations are severely constrained by coarse-grained feature extraction. By reducing complex cloud structures to binary sky-cloud masks, existing visual models fail to account for fine-grained attributes such as cloud scale, color, and radiation source interactions. This oversight introduces an irreducible error floor in irradiance prediction, particularly during the passage of translucent or multi-layered cloud formations. Second, to address single-modal limitations, the field has moved toward multimodal fusion. However, contemporary fusion architectures typically extract spatial and temporal features in isolation, employing “late fusion” strategies that concatenate representations only at the final decision layer. This isolation precludes deep structural coupling, preventing the internal state of one modality from dynamically conditioning the processing of the other. Furthermore, few models explicitly address the hierarchical periodicity inherent in the data, where rigid diurnal cycles are overlaid with stochastic high-frequency noise. There is a distinct lack of architectures capable of simultaneously handling fine-grained visual segmentation, multi-scale temporal periodicity, and deep, low-latency cross-modal fusion.

To resolve these distinct challenges, this research proposes M3S-Net (MultiModal feature fusion network based on Multi-Scale data), a novel architecture designed to achieve high-fidelity ultra-short-term forecasting by unifying fine-grained visual perception with robust multi-scale temporal modeling. Specifically, we introduce three branches of methodological innovations to resolve the identified gaps. Fine-grained visual extraction branch: We propose the Multi-scale Network integrating Partial Channel Selection (MPCS-Net). Unlike binary segmentation methods, MPCS-Net incorporates a Spatial-Channel Selection Mechanism (SCSM) and partial convolutions. This architecture is explicitly designed to model the translucent boundaries and internal texture of clouds, effectively capturing the varying optical depths that drive ramp events. Multi-scale temporal

imaging branch: To handle the complex periodicity of power data, we introduce the multi-scale Sequence to Image analysis Network based on FFT and Retractable attention (SIFR-Net). SIFR-Net utilizes FFT to convert 1D time-series into 2D temporal images, enabling the application of a Retractable Attention (RA) mechanism. This allows the model to dynamically zoom its receptive field, capturing both high-frequency local fluctuations and low-frequency seasonal trends via spectral-temporal disentanglement. Cross-modal mamba fusion branch: We depart from standard Transformer or concatenation fusion by implementing a Multimodal Interaction Fusion (MMIF) module based on Mamba. This module employs a novel “C-matrix swapping” mechanism, where the state-space parameters of the visual stream are exchanged with the temporal stream. This forces the model to decode the visual information conditioned on the temporal state, and vice versa, achieving a true synthesis of modalities with linear computational complexity. Experimental validation on the newly released FGPD and public solar radiation research laboratory (SRRL) datasets demonstrates that M3S-Net significantly outperforms SOTA baselines. These results confirm that deep cross-modal interaction and fine-grained cloud modeling are decisive factors in mitigating the risks of ultra-short-term PV volatility. The main contributions of this paper are summarized as follows.

1. A novel cross-modal mamba fusion framework, M3S-Net, is proposed to overcome the limitations of shallow concatenation in multimodal forecasting with a hierarchical architecture. By introducing a cross-modal Mamba interaction mechanism with a novel “C-matrix swapping” strategy, we enable deep cognitive coupling between visual and temporal modalities. This allows the model to dynamically condition its visual interpretation on the temporal context with linear computational complexity.
2. A multi-scale partial channel selection network, MPCS-Net, is designed to address the inadequacy of binary cloud masks. By integrating a SCSM with partial convolutions, this network explicitly models the translucent boundaries and optical features of clouds. This innovation enables the precise extraction of physically relevant texture features that are critical for quantifying solar irradiance attenuation.
3. A multi-scale sequence to image analysis network, SIFR-Net, based on FFT and retractable attention is introduced to disentangle the complex periodicity of sequence data. By utilizing a sequence-to-image transformation, this module dynamically adjusts its receptive field to capture both high-frequency fluctuations (local cloud transients) and low-frequency trends (diurnal cycles), effectively mitigating performance degradation in longer-horizon forecasts.
4. The introduction and public release of the FGPD dataset. As a significant contribution to the community, FGPD introduces meteorological and power plant data based on the CSRC dataset. Covering various classic weather conditions such as sunny, cloudy,

and overcast, this dataset ensures diversity and establishes a more practical and challenging foundation for advancing ultra-short-term PV power forecasting.

The rest of this paper is organized as follows. Section 2 reviews related studies pertaining to singlemodal and multimodal PV power forecasting. Section 3 details the structural design of the proposed M3S-Net. Section 4 describes the experimental settings and dataset characteristics. Section 5 presents the performance evaluation and comparative analysis. Finally, Section 6 concludes the paper.

2. Related Works

PV power forecasting is a prerequisite for ensuring grid stability, optimizing economic dispatch, and maximizing the hosting capacity of renewable energy systems. As global PV penetration accelerates, the precision of ultra-short-term forecasting has emerged as a critical research imperative. Traditional methodologies, predominantly reliant on singlemodal data sources such as historical power sequences or NWP outputs, often fail to capture the high-frequency variability in irradiance induced by rapid cloud dynamics. Consequently, these conventional models struggle to anticipate “ramp events,” thereby threatening grid inertia and operational security.

In recent years, facilitated by advancements in deep learning technologies and multimodal data fusion methodologies, researchers have begun to synthesize multi-source information integrating GCI, meteorological time-series data, and historical power records to augment forecasting precision. This section provides an exhaustive review of existing research progress, categorized into single-modal data forecasting methods, multimodal data fusion forecasting methods, and relevant datasets.

2.1. Singlemodal Data PV Power Forecasting Methods

Foundational investigations into PV power forecasting were predicated on unimodal data inputs, utilizing either historical generation records or meteorological parameters. These approaches typically exploit the temporal autocorrelation of power output or the physical correlation between atmospheric variables and irradiance. A significant evolution in capturing temporal dependencies involves the application of Bi-GRU. Dai et al. introduced a hybrid ensemble framework optimized via Bi-GRU, achieving a reduction in MSE of approximately 60.4% [11]. By processing temporal sequences in both forward and backward directions, this architecture effectively captures bidirectional dependencies often overlooked by standard RNNs. Parallel to architectural innovations, Wang et al. proposed a system integrating feature selection with multi-objective optimization, enhancing model stability [12]. Addressing the limitations of deterministic forecasting in modeling the stochastic “texture” of PV generation, Huang et al. deployed a conditional generative adversarial network. Furthermore, representing a shift toward continuous-time modeling, Huang et al. also

introduced a multi-stage attention neural network based on neural ordinary differential equations [13]. This architecture optimizes LSTM networks and TCN to perform fine-grained feature extraction, effectively modeling the continuous evolution of solar irradiance beyond discrete time steps.

Distinct from time-series methods, visual approaches utilize GCI to directly observe the primary driver of PV volatility: cloud cover and motion. By analyzing the sky, these models attempt to bypass the lag inherent in time-series data. Foundational work in this domain focuses on mapping visual features directly to irradiance levels. Trigo-Gonzalez et al. developed artificial neural network and support vector machine models utilizing GCI to predict global horizontal irradiance (GHI) [14]. Moving towards end-to-end deep learning, Feng et al. developed two deep CNN models specifically for intra-hour forecasting using only GCI [15]. To explicitly model the kinematics of clouds, Eglik et al. combined computer vision techniques with deep learning, integrating Shi-Tomasi feature detection, the Lucas-Kanade optical flow method, and LSTM networks for solar radiation prediction [16]. Bridging signal processing and computer vision, Liu et al. proposed a sky image-driven deep decomposition method. This novel framework processes GCI to guide the decomposition of the PV power sequence into trend and seasonal components [17]. Representing the SOTA in spatiotemporal feature fusion, Zang et al. introduced a dual-stream network equipped with a PV-guided attention mechanism [18].

Despite the significant accuracy achieved by single-modal methods, they often fail to capture the complex, multi-scale dynamics of PV generation, which are influenced jointly by meteorological trends and cloud dynamics. This limitation has necessitated the development of proposed multimodal data fusion techniques. By leveraging both the temporal precision of historical data and the spatial context of sky imagery, these fused models aim to utilize complementary information to enhance forecasting robustness and accuracy.

2.2. Multimodal Data PV Power Forecasting Methods

To surmount the inherent limitations of unimodal forecasting methodologies, contemporary research has increasingly pivoted towards multimodal data fusion technologies that synthesize ground-based cloud imagery with meteorological parameters and historical power generation data. The seminal work by Kong et al. established a cornerstone in this domain, proposing hybrid architectures such as CNN-LSTM and ConvLSTM to model cloud movement as a spatiotemporal phenomenon [19]. Building upon the unidirectional LSTM approach, Dolatabadi et al. developed a hybrid model combining CNN with Bi-directional LSTM [20]. Moving beyond point forecasting, Terrén et al. introduced a deterministic and Bayesian multi-task deep learning model [21]. Caldas et al. pioneered a method that tightly couples ground-based cloud maps with real-time irradiance

data [22]. Liu et al. approached the problem from a computer vision perspective, employing Sparse Spatiotemporal Descriptors equipped with spatial pyramid pooling [23].

The most recent wave of literature marks a transition from standard CNN-RNN architectures to advanced formulations involving Transformers, TimesNet, and sophisticated clustering algorithms. Wu et al. proposed a structured approach utilizing a CNN coupled with an image RGB matrix analysis to manage sky diversity [24]. They introduced a clustering boundary correction algorithm to classify full-sky images into four distinct meteorological categories. Li et al. addressed the modality gap between 1D time-series and 2D images using TimesNet. The deep features from the ground-based cloud maps (via T2T-ViT) are fused with the temporal features to construct a multimodal feature learning model for ultra-short-term solar irradiance prediction [25]. Dou et al. proposed a multimodal deep clustering architecture that performs collaborative multimodal feature learning and clustering assignment simultaneously [26]. A multimodal fusion module integrates the learned features, and a specialized predictor outputs radiance values conditioned on the identified weather cluster. Zhu et al. proposed a hybrid model for direct normal irradiance (DNI) prediction [27]. The CNN module incorporates dilated convolution to expand the receptive field, and coordinate attention to focus the spatial locations. Innovative transformation techniques have also been explored to enhance feature extraction. Wei et al. introduced the NUTF method, proposing a technique to convert time-series data into an image mode [28]. The fused features from this “time-image” and the actual ground-based cloud image generate GHI using fuzzy logic method. Furthermore, Nie et al. utilized gray-level co-occurrence matrices and local binary patterns to capture texture features [29]. These features are combined with classification features from an improved ConvNeXt network and cloud occlusion factors, and then processed by an SVM-Informer model. Ma et al. adopted a stacking ensemble strategy that ensemble integrates random forest and XGBoost with LSTM and GRU [30]. Wei et al. proposed a hybrid framework fusing discrete wavelet transform that decomposes the non-stationary power series into multiple frequency components, CNN, and LSTM, optimized by the bald eagle search algorithm [31]. Xiang et al. focused on the changing relationships between weather and power [32]. They proposed a dynamic meteorological correlation integrated hybrid method combining XGBoost and temporal convolutional networks. Shi et al. developed CloudMViT, a hybrid architecture integrating CNNs with MobileViT [33]. The specialized cmv2 module efficiently extracts local features while maintaining a low computational footprint, facilitating real-time inference on resource-constrained hardware. Yong et al. introduced the LSEConvNeXt module combining low-rank atrous spatial pyramid pooling with ConvNeXt to significantly improve the pixel-wise segmentation of cloud images [34]. The proposed ConvODE-Mixer framework integrates neural ordinary differential equations with ground-based cloud maps to improve the accuracy of PV power forecasting. Shi et al.

proposed a dual-branch architecture. One branch utilizes a CNN to extract local features, while a parallel branch uses a Transformer to extract global features [35]. A dedicated fusion module integrates these outputs to achieve a comprehensive feature extraction.

Despite the effective progress achieved by the aforementioned methods in PV power forecasting, many existing multimodal fusion methodologies rely on simple feature concatenation or linear fusion mechanisms. They often lack deep cross-modal interaction and adaptive multi-scale feature extraction capabilities. Furthermore, very few models explicitly address the hierarchical and periodic characteristics inherent in meteorological and power data.

2.3. Datasets for Multimodal PV Forecasting

The establishment of standardized benchmarking datasets has been fundamental to the comparative evaluation of solar forecasting algorithms. These repositories, characterized by their temporal continuity and instrumental diversity, serve as the ground truth for validating model generalization.

The solar radiation research laboratory, operated by the U.S. national renewable energy laboratory (NREL) in Golden, Colorado, provides a foundational benchmark for multimodal analysis [36]. Central to the SRRL’s imaging capabilities is the ASI-16 model. The instrument generates RGB channel sky images with a resolution of 1526×1526 pixels. The standard archival resolution for the dataset is typically set to a 10-minute interval. Complementing the optical data is a suite of meteorological measurements sampled at a significantly higher temporal resolution of 60 seconds. These features include: zenith angle, relative humidity, total cloud cover, ambient temperature, average wind speed, wind direction, precipitation, and snow depth. The Folsom dataset originated from Folsom, California. The dataset captures sky images at a 1-minute sampling interval during daylight hours, utilizing a fisheye camera system that produces images with a resolution of 1536×1536 pixels [37]. The dataset provides 1-minute average values of GHI, derived from two Licor LI-200SZ pyranometers. In addition to irradiance and imagery, the Folsom repository includes a comprehensive array of correlated meteorological variables such as ambient temperature, wind speed, and humidity. The SIRTA dataset is collected at the Site Instrumental de Recherche par Télédétection Atmosphérique observatory in Palaiseau, France [38]. Data acquisition at SIRTA is performed at a 1-second sampling interval, which is then aggregated to provide 1-minute average values. Sky images at SIRTA are captured at a resolution of 768×1024 pixels with a 1-minute sampling interval.

While public benchmarking datasets facilitate algorithmic development, dedicated engineering datasets are constructed to address specific operational challenges. The Gansu power grid dataset (GPGD) [34] represents a significant contribution to the study of large-scale renewable energy integration in China. Located in a region with high solar resource availability but complex grid dynamics, the GPGD encompasses meteorological features and power generation

data from seven distinct PV power stations. Utilized by Ma et al. [30], the dataset is situated in Baoying County, Jiangsu Province, representing a plain/coastal climatic zone distinct from the mountain or high-altitude/desert environments of the other datasets. The dataset integrates three months of continuous meteorological data, ground-based cloud imagery, and PV power generation records. The flat terrain of Baoying contrasts with the mountain dataset, shifting the forecasting focus from topographic effects to pure cloud advection and formation processes driven by frontal systems or local convection.

To support the visual reasoning capabilities of forecasting models, research institutions have developed datasets specifically annotated for segmentation and classification tasks. The whole sky image segmentation (WSISEG) and Singapore whole sky nycthemeron image segmentation (SWINySEG) databases are foundational for pixel-level cloud detection. Comprising 400 annotated whole-sky images, the WSISEG dataset provides pixel-level labels for cloud, sky, and undefined regions [39]. SWINySEG extends the scope to 6,768 images, incorporating both daytime and nighttime scenes [40]. Published by Tianjin Normal University, the ground-based cloud dataset (GCD) and ground-based remote sensing cloud database (GRSCD) focus on cloud type classification rather than just segmentation [33]. These datasets provide annotated images covering seven distinct cloud types. Recent advancements have pushed beyond simple classification toward fine-grained attribute analysis, addressing the limitation that binary masks cannot capture the optical depth or physical scale of cloud formations. Constructed by Shi et al. [35], this dataset addresses the unique challenges of mountain PV stations. A pivotal innovation of this dataset is the reclassification of clouds into five distinct categories based on their radiative characteristics, cloud morphology, and associated meteorological features. The dataset features synchronized acquisition of total irradiance, direct irradiance, wind speed, temperature, humidity, atmospheric pressure, and actual power output. Introduced by Niu et al. [41], the CSRC dataset represents a significant leap in granularity. It includes pixel-level annotations for fine-grained cloud attributes, such as scale (size of cloud features), color (spectral properties related to optical depth and water content), and radiation source information. Existing ground-based cloud imagery datasets are predominantly limited to a binary classification distinguishing cloud entities from the sky background, thereby neglecting critical features regarding cloud scale, morphology, and chromatic characteristics. Such coarse-grained representations are insufficient for capturing the nuanced impact of distinct cloud types on solar irradiance and fail to meet the stringent requirements of ultra-short-term forecasting models for high-spatiotemporal-resolution cloud information.

3. Proposed Method

This section delineates the mathematical formulation of the ultra-short-term PV power forecasting problem and

presents the comprehensive architecture of the proposed M3S-Net. Subsequent subsections detail the network's three synergistic components: the fine-grained visual extraction branch, the multi-scale temporal imaging branch, and the cross-modal Mamba fusion branch.

3.1. Problem formulation and overall architecture

Addressed as a sequence-to-sequence regression problem, ultra-short-term PV power forecasting requires the precise mapping of historical multimodal inputs to future power generation over a specified horizon. Achieving this objective necessitates the effective integration of heterogeneous data sources, specifically high-dimensional ground-based cloud imagery and scalar time-series variables. To reconcile the dimensionality disparities between these modalities, the proposed framework incorporates a robust alignment mechanism prior to multi-scale feature extraction. Formally, we define a historical observation window spanning from time step t to T . The forecasting task aims to predict the PV power output for the subsequent τ steps. This process is mathematically formulated as:

$$\begin{aligned} S_t^T &= [S_t, S_{t+1}, \dots, S_T] \\ I_t^T &= [I_t, I_{t+1}, \dots, I_T] \\ M_t^T &= [M_t, M_{t+1}, \dots, M_T] \end{aligned} \quad (1)$$

$$\begin{aligned} I_{T+1}^{T+\tau} &= [I_{T+1}, I_{T+2}, \dots, I_{T+\tau}] \\ &= F(S_t^T, I_t^T, M_t^T, \{\theta\}) \end{aligned} \quad (2)$$

where $S_t^T \in \mathbb{R}^{(T-t+1) \times H \times W \times C}$ represents the ground-based cloud image sequence, with H , W , and C denoting height, width, and channel depth, respectively. $I_t^T \in \mathbb{R}^{T-t+1}$ denotes the historical solar irradiance data. $I_{T+1}^{T+\tau} \in \mathbb{R}^\tau$ denotes the predicted irradiance. $M_t^T \in \mathbb{R}^{T-t+1}$ denotes the historical meteorological data encompassing m parameters. The proposed model and its hyperparameters are designated as $F(\cdot)$ and $\{\theta\}$, respectively. Fig. 1 illustrates the overall flowchart of the proposed M3S-Net. The framework accomplishes the prediction task through three core components.

1. Fine-grained visual extraction branch: The MPCNS-Net is proposed to extract fine-grained spatial features. It employs a dedicated encoder-decoder architecture to explicitly model multi-scale cloud characteristics and translucent boundaries via a spatial-channel selection mechanism.
2. Multi-scale temporal imaging branch: The SIFR-Net is introduced to handle the inherent periodicity of power generation, this branch converts 1D time-series data into 2D representations using FFT. A retractable attention mechanism is then applied to analyzing multi-scale seasonal and trend features.
3. Cross-modal mamba fusion branch: The MMIF module facilitates the deep interaction of multimodal data. Utilizing a cross-modal mamba architecture, it integrates complementary long-range dependencies

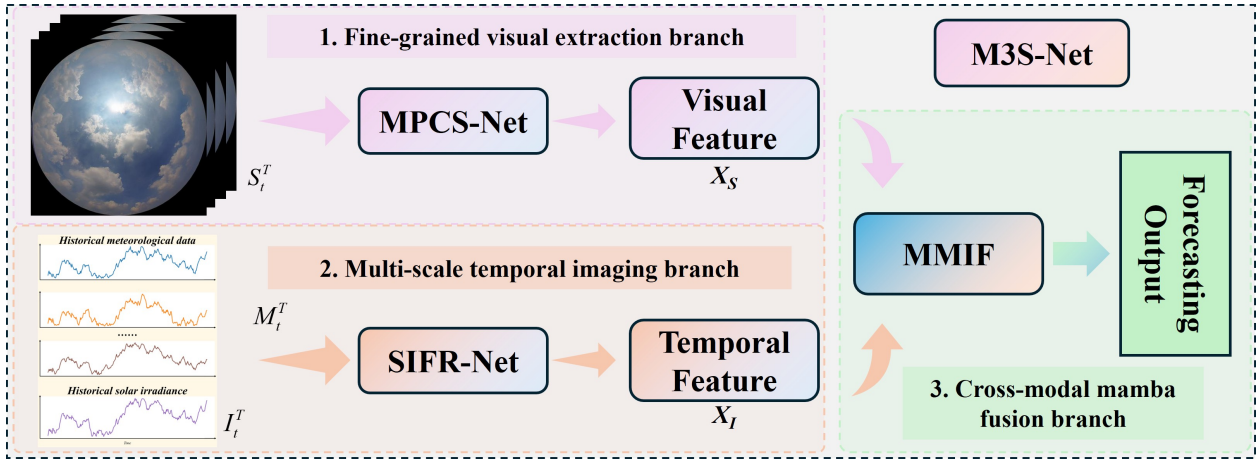


Fig. 1: The overall diagram of the proposed M3S-Net. The framework accomplishes the prediction task through three core components: 1. Fine-grained visual extraction branch; 2. Multi-scale temporal imaging branch; 3. Cross-modal mamba fusion branch.

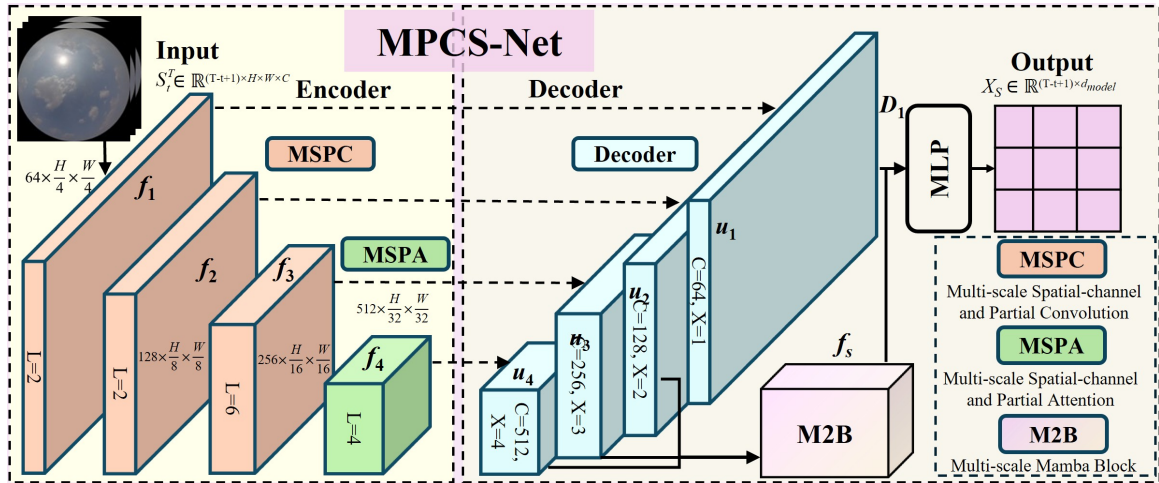


Fig. 2: The structure of the proposed MPCs-Net, which is an Encoder-Decoder architecture. The spatial-channel selection mechanism is embedded within the encoder to form the MSPC and MSPA.

by exchanging output projection matrices between modalities, subsequently generating forecasts via a decoding layer.

3.2. Fine-Grained Visual Extraction Branch Based on MPCs-Net

Accurate segmentation of GCI is a prerequisite for precise PV power forecasting, as the optical properties and distribution of clouds directly govern solar irradiance variability. Cloud formations exhibit complex multi-scale characteristics and translucent boundaries that challenge conventional segmentation approaches. To address these complexities, we propose the MPCs-Net. Building upon the architecture of MPCM-Net [41], which explicitly integrated partial attention convolution with Mamba for efficient global context modeling, MPCs-Net introduces a spatial-channel selection mechanism to further refine multi-scale feature extraction.

While the previously established MPCM-Net demonstrated efficacy in capturing boundary details, its reliance on

atrous convolution for multi-scale fusion limited the interaction between features at different resolutions. The proposed SCSM overcomes this deficiency by adaptively filtering and enhancing informative features across both spatial and channel dimensions. This mechanism allows the network to dynamically prioritize relevant cloud attributes, such as radiation source intensity and spectral variations, thereby significantly improving segmentation accuracy under complex weather conditions.

3.2.1. The Encoder of the MPCs-Net

As depicted in Fig. 2, the MPCs-Net encoder comprises four consecutive convolutional stages. Diverging from previous methodologies (MPCM-Net), the SCSM is embedded within all four stages: the first three utilize the multi-scale spatial-channel and partial convolution (MSPC) block, while the final stage employs the multi-scale spatial-channel and partial attention (MSPA) block. This configuration augments

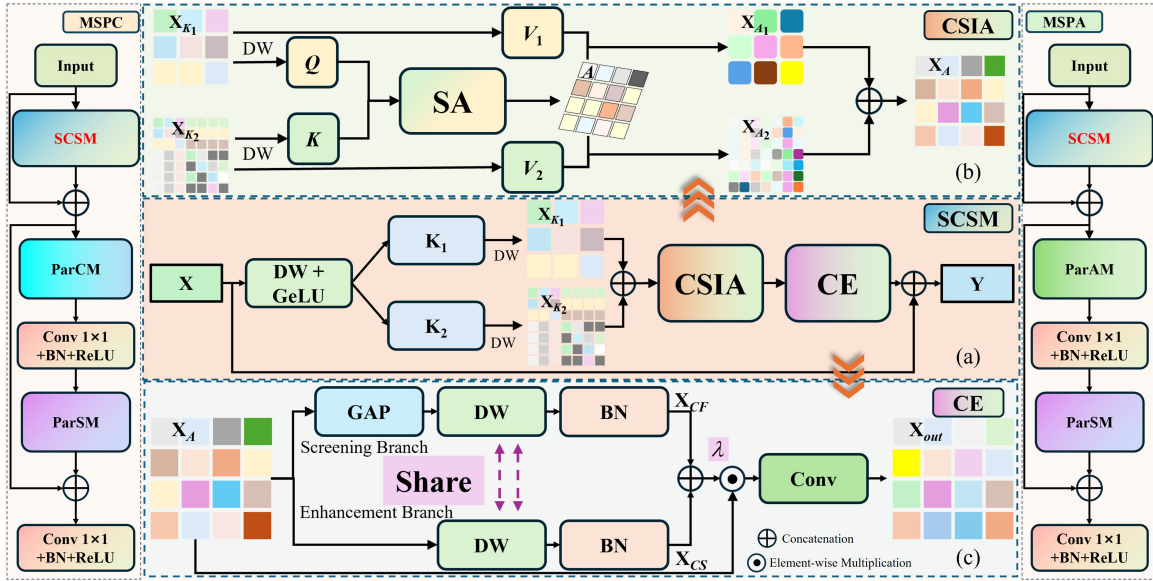


Fig. 3: The structure of the proposed MPCS and MSPA, which is concluding the (a) SCSM. The core modules of the SCSM are (b) CSIA and (c) CE.

the encoder's capacity to adaptively extract multi-scale features and capture inter-channel dependencies. We denote the feature map of the i -th layer as f_i ($i \in \{1, \dots, 5\}$), with dimensions $2^{i-1} \cdot 64 \times (H/2^i) \times (W/2^i)$ ($i \in [1, 2, 3, 4, 5]$).

3.2.2. Spatial-Channel Selective Module

Accurate segmentation under complex weather conditions relies on the effective capture of multi-scale contextual information. Existing multi-scale atrous convolution pyramid methods, as noted in a previous study, typically concatenate feature maps from different scales, often neglecting the interoperability of partial spatial and channel characteristics. To overcome this limitation, we introduce a SCSM within the MPCM-Net framework. As illustrated in Fig. 3, the SCSM introduces a cross-scale interaction attention (CSIA) mechanism. By activating and selecting salient cross-scale feature tokens, this mechanism enhances inter-scale interaction within the encoder. Furthermore, a channel excitation (CE) module [42] is integrated to suppress irrelevant channels and capture region-specific patterns via a self-sharing mechanism, thereby efficiently emphasizing critical inter-regional features.

The initial phase of the MPCS-Net pipeline is dedicated to constructing a rich feature representation that balances computational efficiency with semantic depth. As illustrated in Fig. 3 (a), the input feature tensor X is processed through a depthwise (DW) Convolution layer coupled with a gaussian error linear unit (GeLU) activation function. The strategic selection of DW convolution decouples spatial filtering from channel mixing, substantially reducing floating-point operations (FLOPs) relative to standard convolution. Concurrently, the adoption of GeLU over the traditional ReLU is pivotal. Its smooth, probabilistic approximation of the rectifier facilitates superior gradient flow and enhances

non-linear representation capabilities in deep architectures. This configuration ensures high feature extraction efficiency while preserving the non-linear capacity required to model the complex scattering functions of cloud particles. To enable adaptive focus on relevant spatial contexts, essential for extracting cloud clusters of varying scales, the architecture employs explicitly decomposed convolutions. We utilize convolution kernels of differing scales to selectively extract spatial features, generating scale-specific feature maps, X_{K_i} . This operation is formally expressed as: $X_{K_i} = DW(K_i)$, where i represents the index of large-scale convolution kernels. Consistent with established methodologies in recent literature [43], this strategy exploits the interplay between kernel size and dilation rate. By progressively increasing these parameters, the explicitly decomposed operations synthesize receptive fields of diverse magnitudes, enhancing the network's multi-scale representation capability without the parameter proliferation associated with standard large-kernel convolutions.

MPCS-Net introduces CSIA that is designed to facilitate sophisticated information exchange between feature maps characterized by different receptive fields. As shown in Fig. 3 (b), we employ an asymmetric projection strategy where the Query (Q) and Value (V_1) vectors are derived from the low-scale feature map X_{K_1} , while Key (K) and Value (V_2) vectors are derived from the high-scale feature map, X_{K_2} . This asymmetric projection leverages the hierarchical local features of the image to guide the information interaction. The high-level context (X_{K_2}) acts as the key to unlock the relevant details in the low-level query (X_{K_1}). The process is mathematically described by the following equations:

$$Q = DW(X_{K_1}), K = DW(X_{K_2}) \quad (3)$$

$$V_1 = DW(X_{K_1}), V_2 = DW(X_{K_2}) \quad (4)$$

$$A = \text{Softmax} \left(\frac{QK^T}{\sqrt{d_k}} \right) \quad (5)$$

where A represents the attention score matrix, encapsulating the interactive information between scales. To achieve dynamic, adaptive extraction of multi-scale cloud systems, the feature maps derived from the decomposed large-kernel sequence are weighted and fused using these interaction scores. This yields the multi-scale spatially selected feature tensor, X_A :

$$X_{A_1} = A \odot V_1, X_{A_2} = A \odot V_2 \quad (6)$$

$$X_A = \text{Cat} \left(X_{A_1}, X_{A_2} \right) \quad (7)$$

where \odot denotes the element-wise multiplication, $\text{Cat}(\cdot)$ denotes the concatenation. This formulation ensures that the fused features X_A are not merely a summation of scales, but a context-aware synthesis where global cloud patterns inform the interpretation of local pixels.

Recognizing that different spectral channels emphasize distinct image regions (e.g., solar luminance vs. cloud texture), we propose the CE module to dynamically modulate channel importance. As depicted in Fig. 3, the fused feature tensor X_A is bifurcated into a screening branch (to filter noise) and an enhancement branch (to amplify discriminative features), yielding X_{CF} and X_{CS} , respectively. The final output of the CE module is obtained by aggregating the original input X_A with the outputs of these two branches. The mechanism incorporates a shared, learnable parameter λ , which adaptively regulates the information flow:

$$X_{out} = \text{Conv} \left(X_A \odot (\lambda \cdot \text{Cat}(X_{CS}, X_{CF})) \right) \quad (8)$$

where \cdot denotes the multiplication. This self-calibrated extraction mechanism effectively suppresses channel redundancy while highlighting critical cloud layer details.

3.2.3. The Decoder of the MPCS-Net

The decoder maintains structural consistency with our previous work but reformulates the final output as a context vector to ensure seamless integration with the multimodal fusion process. Specifically, as illustrated on the right side of Fig. 1, the decoder employs a recursive upsampling and concatenation strategy to generate multi-scale features u_i . These features are aggregated into a composite representation, which is processed by a M2B to produce f_s . Finally, f_s is upsampled and concatenated with u_1 to generate D_1 . The D_1 undergoes dimensionality reduction via a multi-layer perceptron (MLP), yielding the visual feature mapping $X_S \in \mathbb{R}^{(T-t+1) \times d_{model}}$, where d_{model} denotes the dimensionality of the network.

3.3. Multi-scale Temporal Imaging Branch Based on SIFR-Net

PV power generation is governed by complex temporal dynamics characterized by the coupling of long-term climatic trends, daily solar cycles, and transient meteorological fluctuations. Standard Transformer architectures [44], while effective for sequence modeling via self-attention, often struggle to explicitly disentangle these multi-scale periodicities from localized disturbances. This limitation hinders the construction of representation spaces capable of simultaneously capturing global trends and local dynamics. To mitigate this limitation, we introduce SIFR-Net, a multi-scale Sequence to Image analysis network that systematically integrates FFT with a retractable attention mechanism [45].

3.3.1. Multi-Scale Pyramid Construction

The module accepts multivariate time-series data $X_0 \in \mathbb{R}^{L \times (m+1)}$, comprising historical meteorological parameters and solar irradiance. Inspired by the hierarchical feature maps utilized in Swin Transformers [46], we construct a multi-scale representation $\mathcal{X} = \{X_0, X_1, \dots, X_M\}$ through progressive downsampling, where X_m represents the sequence at the m -th scale with resolution $L/2^m$, as shown in Fig. 4. This multi-scale pyramid architecture enables the model to discern temporal dynamics ranging from fine-grained short-term fluctuations to coarse-grained long-term trends.

To capture nonlinear interdependencies among variables, we implement a channel-wise self-attention (CSA) mechanism at the coarsest scale X_M . Fig. 5 illustrates the process. Specifically, given that X_M possesses the shortest sequence length, it effectively encapsulates global contextual information, rendering it ideal for modeling cross-variable interactions. This process can be expressed as:

$$X_M^E = \text{CSA} (Q_M, K_M, V_M) \quad (9)$$

where Q_M , K_M and V_M are derived from X_M via linear projections. The processed sequences are subsequently projected into a unified feature space via a shared embedding layer:

$$\mathcal{X}_E = \{X_0^E, X_1^E, \dots, X_M^E\} = \text{Embedding} (\mathcal{X}) \quad (10)$$

where $X_m^E \in \mathbb{R}^{[L/2^m] \times d_{model}}$. This design enables the model to adaptively learn and weight the dependencies among different meteorological and power variables, producing more discriminative fused features and laying a foundation for subsequent periodicity and trend decomposition.

3.3.2. FFT-based 2D Transformation and Retractable Attention

A core innovation of SIFR-Net is the transformation of 1D temporal sequences into 2D tensors to leverage image-based attention mechanisms. The sequence and image processing flow is shown in Fig. 6. First, an FFT is applied to

X_M^E to identify the top- k dominant frequencies and their corresponding periods $\{p_1, p_2, \dots, p_k\}$, generating k two-dimensional tensors accordingly. Based on these periods, sequences at all scales are reshaped into 2D tensors $\mathbf{Z}_m^{(k)} \in \mathbb{R}^{p_k \times f_{m,k}}$, where the column dimension $f_{m,k}$ adapts to the sequence length at scale m . This restructuring naturally separates intra-period variations (mapped to rows) from inter-period evolution (mapped to columns). In total, the sequence set \mathcal{X} is converted into $(m+1) \times k$ multi-resolution images.

Then, to effectively model the superposition of local fluctuations and global trends within these 2D representations, we propose a RA module. While the axial attention mechanism adopted in the literature [47] offers one approach to decoupling, its receptive field is relatively fixed. A rigid axial decomposition may fail to adaptively capture cross-scale dependencies that are not strictly aligned with the image rows/columns, or that reside in specific sparse locations. In contrast to rigid axial attention, our method offers a dynamic, “scalable” receptive field through two alternating blocks.

Specifically, as illustrated in Fig. 6 (b1) and (b2), the module processes the input 2D temporal image $\mathbf{Z}_m^{(k)}$ through two alternately stacked attention blocks. The dense attention block (D-MSA) employs local window self-attention. The 2D image is partitioned into non-overlapping $W \times W$ windows, and standard self-attention is computed within each window. This allows the model to focus on relationships among time points within local neighborhoods, capturing high-frequency, short-period seasonal patterns as well as continuous local textures in the image. The computation is formulated as follows:

$$\mathbf{Q}^{(j)}, \mathbf{K}^{(j)}, \mathbf{V}^{(j)} = \mathbf{Z}^{(j)} \mathbf{W}_Q, \mathbf{Z}^{(j)} \mathbf{W}_K, \mathbf{Z}^{(j)} \mathbf{W}_V \quad (11)$$

$$\text{D-MSA}(\mathbf{Z}^{(j)}) = \text{Softmax}\left(\frac{\mathbf{Q}^{(j)} (\mathbf{K}^{(j)})^T}{\sqrt{d_k}}\right) \mathbf{V}^{(j)} \quad (12)$$

where $\mathbf{Z}^{(j)} \in \mathbb{R}^{W^2 \times C}$ within the j -th window, W_* represents learnable projection weights. All window computations are performed in parallel, and the output features are subsequently reassembled into the original image layout.

The sparse attention block (S-MSA) employs a grid-based sparse sampling strategy. Pixels are sampled at fixed intervals I , and global attention is computed among these sparse points. This allows any time point in the image to interact with distant yet potentially semantically relevant points elsewhere. This enables the model to capture long-range dependencies and slowly evolving trends that span across multiple periods. The computation proceeds as follows:

$$\mathbf{Z}_{\text{sparse}} = \text{Gather}(\mathbf{Z}, I) \quad (13)$$

$$\mathbf{Q}_s, \mathbf{K}_s, \mathbf{V}_s = \mathbf{Z}_{\text{sparse}} \mathbf{W}_Q^s, \mathbf{Z}_{\text{sparse}} \mathbf{W}_K^s, \mathbf{Z}_{\text{sparse}} \mathbf{W}_V^s \quad (14)$$

$$\text{S-MSA}(\mathbf{Z}) = \text{Scatter}\left(\text{Softmax}\left(\frac{\mathbf{Q}_s \mathbf{K}_s^T}{\sqrt{d_k}}\right) \mathbf{V}_s, I\right) \quad (15)$$

where the Gather (\cdot) operation samples features along the spatial dimension at interval I , while Scatter (\cdot) performs the inverse, interpolating the updated sparse features back to their original positions. I is a hyperparameter that controls the “sparsity” and globality of the receptive field. A larger I results in fewer sampled points participating in the computation but enables each point to interact directly with features from more distant locations.

3.3.3. Amplitude-Weighted Fusion and Prediction

After processing by the retractable attention module, a refined 2D feature map $\mathbf{Z}_m^{(k)} \in \mathbb{R}^{p_k \times f_{m,k} \times C}$ is obtained for each scale m and each period k . Then the 2D feature maps are flattened back into 1D sequences. We perform a reshaping operation inverse to the imaging process:

$$\mathbf{x}_m^{(k)} = \text{Reshape}_{2D \rightarrow 1D}(\mathbf{Z}_m^{(k)}) \in \mathbb{R}^{L_m \times C} \quad (16)$$

where $L_m = p_k \times f_{m,k}$ equals the original sequence length at scale m , thereby ensuring temporal alignment. To synthesize the information extracted from different periodic views, we employ an amplitude-weighted fusion strategy. Specifically, using the amplitude spectrum $\mathbf{A} = \{A_{f_1}, \dots, A_{f_K}\}$ extracted during the imaging phase from the coarsest scale, which reflects the relative importance of each period, normalized weights are computed as:

$$\left\{ \hat{A}_{f_k} \right\}_{k=1}^K = \text{Softmax}\left(\left\{ A_{f_k} \right\}_{k=1}^K\right) \quad (17)$$

then the fused feature \mathbf{h}_m at scale m is given by:

$$\mathbf{h}_m = \sum_{k=1}^K \hat{A}_{f_k} \cdot \mathbf{x}_m^{(k)}, \quad m \in \{0, \dots, M\} \quad (18)$$

This step adaptively enhances the expression of dominant periodic patterns in the features.

Finally, a multi-scale prediction head generates an ensemble forecast $X_I \in \mathbb{R}^{(T-t+1+\tau) \times d_{\text{model}}}$, integrating contributions from all scales to ensure robustness against both high-frequency noise and long-term drift.

$$X_I = \text{Ensemble}(\text{Head}_0(\mathbf{h}_0), \dots, \text{Head}_M(\mathbf{h}_M)) \quad (19)$$

3.4. Multi-model Fusion Branch Based on Mamba

The preceding branches provide two distinct representations of the PV system state: spatial features capturing cloud topology ($X_S \in \mathbb{R}^{(T-t+1) \times d_{\text{model}}}$) and temporal features encoding periodic power dynamics ($X_I \in \mathbb{R}^{(T-t+1+\tau) \times d_{\text{model}}}$). Conventional fusion techniques, such as simple concatenation or linear superposition, often fail to model the dynamic, time-varying interactions between these modalities, particularly over long sequences where dependencies may shift rapidly. To overcome this limitation, we introduce the MMIF module, underpinned by the Mamba architecture.

3.4.1. Multimodal Interaction Fusion

As a selective state-space model [48], Mamba offers the advantages of linear complexity and global receptive fields when processing long sequences. Its core mechanism lies in the dynamic generation of model parameters (e.g., \overline{B} , \overline{C} , and Δ) based on the input, enabling selective retention and propagation of critical information. To facilitate deep interaction between the two modalities, we introduce a cross-modal ‘‘C-matrix swapping’’ mechanism. While recent works like Sigma and STT [49, 50] have explored parameter exchange in Mamba for static multimodal image segmentation, M3S-Net uniquely adapts this mechanism to the spatiotemporal domain. Unlike Sigma and STT, which align spatially registered modalities (e.g., RGB-Thermal), our approach aligns high-frequency temporal dynamics with spatial cloud features, addressing the specific challenge of time-lagged causality in PV forecasting.

Specifically, as illustrated in Fig. 7, the sequence of each modality is fed into a Mamba block that shares the same basic structure. When computing the output, we swap the \overline{C} matrices (the state-to-output mapping matrices) generated by each modality. As a result, each modality produces its output by relying not only on its own historical state but also on contextual information embedded in the state of the other modality. This process can be formally expressed as follows:

$$h_S^k = \overline{A}_S h_S^{k-1} + \overline{B}_S x_S^k \quad (20)$$

$$y_S^k = C_I h_S^k + D_S x_S^k \quad (21)$$

$$h_I^k = \overline{A}_I h_I^{k-1} + \overline{B}_I x_I^k \quad (22)$$

$$y_I^k = C_S h_I^k + D_I x_I^k \quad (23)$$

where k denotes the sequence position index, h represents the hidden state, and \overline{A} , \overline{B} , D are the parameterized matrices specific to each modality. The key step lies in the fact that the output y_S^k of the ground-based cloud image modality X_S utilizes the mapping matrix C generated by the temporal modality X_I , and vice versa. This design forces the model to integrate the feature patterns extracted by the other modality when decoding the current information of each modality. Consequently, tight cross-modal correlations are established across all positions of the sequence, enabling genuine end-to-end information interaction.

3.4.2. Feature Fusion and Decoding Prediction

Following the cross-modal interaction, the mutually informed output sequences Y_S and Y_I are concatenated and projected via a linear layer to form the unified fusion feature H_{fusion} . A lightweight Transformer decoder then autoregressively generates the final PV power forecast. This decoder captures the dependencies within the fused representation, mapping the synthesized cross-modal context to the precise power output values for the target horizon.

$$H_{fusion} = \text{Linear}(\text{Cat}(Y_S, Y_I)) \quad (24)$$

Table 1

Cloud classification standard for CSRC dataset.

Cloud class	Shape and characteristic	Color
White cloud	White transparent clouds, such as cirrus and cirrocumulus, are pure white and translucent or appear as white scaly flakes.	White
Gray cloud	Gray clouds, such as stratus and altostratus, are gray and foggy with a dark base.	Gray
Sun	Radiation source	Red
Background	There are no clouds in the sky	Blue

4. Experimental Setting

The experimental framework was established using Python 3.9 within the PyTorch 1.10.1 ecosystem, providing a robust environment for DL deployment. To accommodate the computational intensity of multimodal feature fusion, all training and evaluation procedures were executed on a high-performance server running Ubuntu 21.04. The hardware infrastructure consisted of an Intel(R) Xeon(R) Gold 5218N CPU clocked at 2.3 GHz and an NVIDIA GeForce RTX 4090 GPU, equipped with 24 GB of VRAM to support large-scale tensor operations. The remainder of this section contains the dataset, evaluation metrics, and baseline models.

4.1. Dataset

PV power forecasting accuracy is inextricably linked to the fidelity and informational density of the input variables. Singlemodal time-series data inevitably prove insufficient for characterizing the direct modulation of surface solar irradiance by dynamic sky conditions, particularly those driven by stochastic cloud kinematics. In the context of ultra-short-term forecasting, rapid cloud transients, encompassing morphological evolution and abrupt displacement, induce sharp fluctuations in irradiance, which subsequently destabilize PV power output. Consequently, the integration of ground-based cloud imagery, which captures localized atmospheric states with high spatiotemporal resolution, is paramount for enhancing predictive precision.

Existing multimodal datasets for PV forecasting frequently suffer from a critical limitation: ground-based cloud imagery is often reduced to binary masks distinguishing only between cloud and sky, thereby neglecting critical attributes such as cloud scale, morphology, and color features. Such coarse-grained representations are inadequate for satisfying the stringent requirements of ultra-short-term forecasting models, which demand high-fidelity environmental data.

Addressing this deficiency, our prior research introduced a novel ground-based cloud image dataset that incorporates complex-scale attributes along with radiation source and color characteristics [41]. This dataset emphasizes cloud scale and color properties and introduces fine-grained segmentation of clouds based on radiation sources, stratifying datasets into four distinct classes (details in Table 1).

The observational infrastructure was deployed in Xiqing District, Tianjin, China (Geographic coordinates: 117.03° E, 39.10° N). Visual data were acquired using an All-Sky Imager (ASI-DC-TK02), encased in a weather-resistant enclosure and offering a field of view exceeding 180°. The device was calibrated to capture sky images at fixed 30-second intervals. All imagery is archived in RGB JPEG format with a resolution of 1260 × 1260 pixels. To ensure ground truth reliability, fine-grained annotations were generated by trained meteorologists utilizing LabelMe software, with subsequent cross-validation performed to guarantee label consistency. This dataset facilitates the pixel-wise quantification of sunlight attenuation by varying cloud types, serving as a foundational resource for mapping multimodal inputs to PV generation.

Complementing the visual data, our proposed Fine-Grained PV Power Dataset integrates high-frequency meteorological records with PV power output. Meteorological parameters were logged by an on-site weather monitoring station at 10-minute intervals, synchronized with the imaging frequency. The monitored variables include: GHI (W/m²), DNI (W/m²), diffuse horizontal irradiance (DHI, W/m²), wind speed (WS, m/s), wind direction (WD, °), temperature (T, °C), relative humidity (RH), and atmospheric pressure (P, Pa). Data collection spanned the full calendar year of 2025 (January 1 to December 31), encompassing a diverse array of meteorological conditions, including sunny, cloudy, and overcast, to ensure temporal representativeness. Fig. 8 elucidates the synchronous fluctuations of these meteorological data streams on a representative day, visually corroborating the coupling between cloud dynamics and irradiance attenuation.

The aggregate dataset encompasses 59 sunny days, 191 cloudy days, and 50 overcast days. To optimize training efficiency and model generalization, a selective filtration strategy excluded the majority of monotonic sunny and stable overcast data points, which contain limited informational variance. Conversely, a higher proportion of partly cloudy data was retained. This strategy effectively reduces dataset volume while compelling the deep learning model to learn robust features associated with complex cloud interactions. Post-alignment of imagery and meteorological sequences, 41,780 valid data points were identified. These were randomly shuffled and stratified into training, validation, and test sets in a 7:1:2 ratio.

4.2. Evaluation Metrics

To facilitate a rigorous assessment of the M3S-Net model's efficacy in PV power forecasting, this study adopts a comprehensive suite of evaluation metrics spanning point-prediction accuracy, trend consistency, and segmentation quality.

Fundamentally, PV power forecasting constitutes a regression problem necessitating measuring the deviation between predicted and observed values. This paper employs the following metrics: MAE, MSE, normalized root mean squared error (NRMSE), and R². MAE quantifies the mean

magnitude of errors without considering their direction, offering intuitive interpretability. MSE heavily penalizes large deviations, serving as a critical indicator for ramp event prediction failure. NRMSE facilitates performance comparison across disparate scales by normalizing the error against the data range. R² indicates the proportion of variance in the dependent variable explained by the model; values approaching 1 denote superior goodness-of-fit. The formulas for these metrics are given below:

$$\text{MAE} = \frac{1}{N} \sum_{i=1}^N |y_i - \hat{y}_i| \quad (25)$$

$$\text{MSE} = \frac{1}{N} \sum_{i=1}^N (y_i - \hat{y}_i)^2 \quad (26)$$

$$\text{NRMSE} = \frac{1}{\max(y) - \min(y)} \sqrt{\frac{1}{N} \sum_{i=1}^N (y_i - \hat{y}_i)^2} \times 100\% \quad (27)$$

$$R^2 = 1 - \frac{\sum_{i=1}^N (y_i - \hat{y}_i)^2}{\sum_{i=1}^N (y_i - \bar{y})^2} \quad (28)$$

where y_i is the true value, \hat{y}_i is the predicted value, \bar{y} is the mean of the true values, and N denotes the sample size.

For ground based cloud image segmentation, standard image segmentation metrics are used, including Precision (P), Recall (R), and Mean Intersection over Union (MIoU). The formulas are:

$$P = \frac{TP}{TP + FP} \quad (29)$$

$$R = \frac{TP}{TP + FN} \quad (30)$$

$$\text{MIoU} = \frac{1}{C} \sum_{c=1}^C \frac{TP_c}{TP_c + FP_c + FN_c} \quad (31)$$

where TP denotes true positives, FP denotes false positives, FN denotes false negatives, and C denotes the number of classes.

During network training, MSE serves as the loss function for the PV forecasting task due to its continuous differentiability and efficacy in gradient descent optimization. Concurrently, binary cross-entropy (BCE) loss governs the optimization of the pixel-wise cloud classification branch.

4.3. Benchmark Models

To benchmark the performance of the proposed M3S-Net, a diverse array of SOTA models was selected for comparison. The fine-grained visual extraction branch is evaluated against both classical semantic segmentation architectures and specialized cloud segmentation networks. These include CNN-based models such as U-Net [51], CloudFU-Net [52], and MPCM-Net [41], alongside Vision Transformer (ViT) architectures like SegFormer [53] and CloudSwinNet [54]. The forecasting capabilities are benchmarked against established time-series models (LSTM [55],

Table 2

Quantitative comparison with different methods on FGPD for GCI segmentation. ↓ (or ↑) indicates lower (or higher) is better. The best results are highlighted in bold.

Method	P(↑)	R(↑)	MIoU(↑)
U-Net	66.7	64.6	46.7
SegFormer	84.6	85.2	61.3
CloudFU-Net	86.9	86.5	62.1
CloudSwinNet	87.1	87.6	62.3
MPCM-Net	90.6	91.1	64.8
MPCS-Net	91.3	91.8	65.6

DLinear [56], and TimesNet [57]) and multimodal fusion frameworks, including CNN-based [58], ViT-based [59], and T2T [25]. All experimental results cited in this study were derived either from open-source implementations or directly from the original authors' publications to ensure a fair and reproducible comparative analysis.

5. Experimental Results and Discussions

To rigorously evaluate the efficacy of the proposed M3S-Net, a comprehensive comparative analysis was conducted against established baseline models for ultra-short-term PV power forecasting. The prediction horizons were stratified from 10 to 60 minutes-ahead (MA), corresponding to 1 to 6 time steps, to assess model performance across varying temporal scales.

5.1. Overall Performance

The quantitative evaluation results of the proposed MPCS-Net and other segmentation methods on GCI of our FPGD. Table 2 demonstrates the superior performance of our proposed MPCS-Net over all comparative GCI segmentation methods on FGPD. Specifically, MPCS-Net achieves MIoU improvements of 0.8%, compared to the previous MPCM-Net [41]. The performance advantage stems from our method, from its CSIA within SCSM, which enhances inter-scale interaction within the encoder, coupled with the CE module that emphasizes critical inter-regional features.

The comparative results between the proposed method and the benchmark models are presented in Tables 3 through 5. M3S-Net consistently demonstrated superior performance across all prediction horizons. Specifically, within the critical 10-minute forecast window, M3S-Net achieved a significant reduction in MAE and NRMSE of approximately 6.2% and 4.8%, respectively, relative to the second-best performing model. Furthermore, the model attained a R^2 of 0.964, indicating exceptional predictive precision. As the prediction horizon extended to 60 minutes, M3S-Net exhibited the slowest rate of performance degradation among all tested models, which corroborates the model's enhanced robustness and stability in longer-term forecasting scenarios.

These comparative experiments elucidate the distinct advantages inherent in fusing multi-source data. Models relying exclusively on time-series data, such as LSTM, DLinear,

and TimesNet, performed adequately under stable meteorological conditions. However, during periods of rapid irradiance fluctuation induced by cloud cover, these single-modal models exhibited significantly increased prediction errors and pronounced phase lag. In contrast, models incorporating ground-based cloud imaging (e.g., CNN-based, ViT-based, and T2T) demonstrated superior overall performance. This disparity validates the hypothesis that spatial distribution and dynamic information derived from cloud images are indispensable for capturing the underlying causality of power fluctuations.

M3S-Net significantly outperformed other multimodal fusion architectures, a success attributable to the synergistic engineering of its three core branches. First, the MPCS-Net facilitates fine-grained extraction of multi-scale cloud features and, crucially, the resolution of semi-transparent cloud boundaries. Second, the SIFR-Net explicitly models the multi-scale periodicity and trends inherent in power data via time-series imaging and scalable attention mechanisms. Third, the MMIF module enables deep feature complementarity and information exchange that far exceeds the capabilities of simple concatenation or linear fusion strategies. Additionally, the bar chart in Fig. 9, which compares the average errors across the 10-to-60-minute horizon, visually underscores that M3S-Net maintains the lowest error magnitude.

To investigate the model's generalization capabilities under diverse meteorological scenarios, the test dataset was stratified into three typical weather categories: sunny, cloudy, and overcast, as shown in Fig. 10 and 11. From the visual results, all models achieved satisfactory predictions under sunny conditions, where solar irradiance is stable and primarily governed by the deterministic solar trajectory. Consequently, temporal models alone suffice for reliable forecasting in these regimes. However, the M3S-Net prediction curve exhibited the tightest alignment with ground truth values and the lowest volatility. This substantiates the SIFR-Net module's precision in extracting long-term stationary trends and diurnal periodic features. During ramping events characterized by rapid irradiance drops and recoveries due to cloud occlusion, multimodal time-series models, such as CNN-based and ViT-based, displayed significant forecasting error. Conversely, as the expansion of the prediction range, M3S-Net exhibits the fastest and most accurate response to steep power ramps, the error reduction of the fitting curve is the least significant compared to other models. This performance enhancement stems primarily from the MPCS-Net's effective capture of fine-grained cloud boundaries and motion dynamics. Under overcast conditions, characterized by low overall irradiance and complex fluctuation patterns, M3S-Net maintained a relatively stable prediction performance. This indicates that its multi-scale feature extraction and fusion mechanisms can effectively adapt to varying irradiance intensities and weather modes.

Table 3Comparison results of GHI based on MAE (W/m^2) on the FGPD.

Model structure	Method	MAE (W/m^2) (\downarrow)					
		10 MA	20 MA	30 MA	40 MA	50 MA	60 MA
Singlemodal	LSTM	39.76	42.28	45.53	48.97	54.64	61.42
	DLinear	22.32	31.44	44.33	55.62	66.73	77.64
	TimesNet	23.45	28.61	34.25	41.27	47.82	55.66
	CNN-based	22.56	27.74	33.96	40.66	47.12	54.12
Multimodal	ViT-based	22.37	28.13	33.84	39.72	47.33	53.83
	T2T	21.16	26.64	32.17	38.43	45.67	53.12
	M3S-Net	19.84	24.43	30.76	37.14	43.51	50.35

Table 4

Comparison results of GHI based on NRMSE (%) on the FGPD.

Model structure	Method	NRMSE (%) (\downarrow)					
		10 MA	20 MA	30 MA	40 MA	50 MA	60 MA
Singlemodal	LSTM	6.82	7.31	7.94	8.82	9.41	10.23
	DLinear	5.14	5.72	7.16	8.73	10.26	11.78
	TimesNet	5.42	5.96	6.78	7.64	8.86	9.35
	CNN-based	5.23	5.88	6.52	7.36	8.29	9.14
Multimodal	ViT-based	5.09	5.63	6.38	7.14	7.93	8.89
	T2T	4.84	5.36	6.03	6.85	7.72	8.68
	M3S-Net	4.61	5.14	5.78	6.56	7.42	8.51

Table 5Comparison results of GHI based on R^2 on the FGPD.

Model structure	Method	R^2 (\uparrow)					
		10 MA	20 MA	30 MA	40 MA	50 MA	60 MA
Single-modal	LSTM	0.912	0.903	0.894	0.882	0.864	0.845
	DLinear	0.931	0.922	0.910	0.897	0.872	0.841
	TimesNet	0.947	0.923	0.904	0.884	0.849	0.807
	CNN-based	0.954	0.931	0.916	0.902	0.874	0.851
Multi-modal	ViT-based	0.953	0.934	0.915	0.894	0.871	0.848
	T2T	0.958	0.945	0.928	0.902	0.885	0.864
	M3S-Net	0.966	0.947	0.931	0.911	0.893	0.872

Table 6

Ablation experimental results on the FGPD.

Version	MAE (W/m^2) (\downarrow)	NRMSE (%) (\downarrow)	R^2 (\uparrow)
A	23.44	5.37	0.948
B	22.46	5.21	0.951
C	22.31	5.15	0.853
D	21.84	5.06	0.957
E	21.45	4.94	0.960
F	20.96	4.72	0.962
M3S-Net	19.84	4.61	0.964

5.2. Ablation Study

To substantiate the necessity and individual contributions of the core components within M3S-Net, a rigorous series of ablation experiments was designed. All trials utilized an identical dataset comprising synchronized GCI and meteorological telemetry, maintaining consistent hyperparameter

configurations to ensure the validity of the comparative analysis. The comparison results for the 10 MA are summarized in Table 6. The experimental design segments the evaluation into six distinct schemes (A through F), each representing a specific architectural hypothesis.

Employing SIFR-Net to process historical power and meteorological data exclusively, we established a baseline (Scheme A) devoid of visual information. The MAE based on this configuration exceeded that of the complete model by approximately 15%. This disparity implies that historical time-series data alone is insufficient for predicting rapid fluctuations induced by cloud movement.

Building upon Scheme A, the fine-grained visual extraction branch was substituted with a standard ResNet-50 (Scheme B) for feature extraction, fusing these visual features with time-series data via concatenation. This approach yielded performance enhancements over Scheme A, where the MAE decreased by approximately 4%, thereby demonstrating the efficacy of incorporating visual data. However, its performance remained significantly inferior to the complete M3S-Net, suggesting that rudimentary feature extraction and fusion methods fail to fully exploit critical visual information or establish deep inter-modal interactions.

Substituting the cloud branch with our prior MPCM-Net architecture (Scheme C) resulted in performance superior to Scheme B but inferior to MPCM-Net equipped with the SCSM (Scheme D). These results indicate that the SCSM module, through its CSIA and CE mechanisms, adaptively enhances the representation of critical cloud features—such as thick cloud regions and motion fronts. Analysis of the

MAE suggests this module contributes approximately 2% to the overall prediction accuracy.

In Scheme E, we utilized the complete MPCs-Net and SIFR-Net but eliminated the multi-scale ensemble prediction head within SIFR-Net, relying solely on the coarsest-scale features for the final forecast. Performance deteriorated, with a marked loss of accuracy in short-term forecasts. This finding substantiates the effectiveness of the multi-scale pyramid structure and ensemble prediction heads: fine-scale heads focus on capturing high-frequency, short-term fluctuations (e.g., gust effects), while coarse-scale heads model long-term trends and diurnal cycles. Their synergistic operation significantly enhances the model's adaptability to dynamics across varying temporal scales.

For Scheme F, we employed the full MPCs-Net and SIFR-Net but replaced the cross-modal Mamba fusion module with feature concatenation followed by a MLP. Experimental results indicate that this configuration performed significantly worse than the complete M3S-Net, with the R^2 for 10 MA forecasts decreasing by more than 0.02. This empirical evidence robustly substantiates the intrinsic value of the proposed cross-modal Mamba interaction mechanism. By exchanging state mapping matrices, this mechanism compels each modality to integrate context provided by the other during self-information decoding. This process facilitates genuine, sequence-wide deep feature complementarity and dependency modeling.

In conclusion, the proposed M3S-Net achieved superior performance across all evaluation protocols, thereby validating the rationality and advancement of the overall architectural design.

5.3. Sensitivity Analysis

To ensure model robustness and provide rigorous guidelines for practical deployment, we conducted a comprehensive sensitivity analysis of key hyperparameters governing the M3S-Net architecture.

First, we investigated the influence of the historical input sequence length, denoted as the lookback window L_x . We evaluated the model's performance with input lengths of 24, 48, 96, and 192 time steps, corresponding to historical horizons of 4, 8, 16, and 32 hours, respectively. As illustrated in Fig. 12, the model achieves optimal predictive accuracy across the majority of forecast horizons when $L_x = 96$ (16 hours).

Subsequently, we examined the effect of the input resolution of ground-based sky images, testing configurations of 64×64 , 128×128 , and 256×256 pixels. The results, presented in Fig. 13, indicate that the impact of resolution is minimal on our M3S-Net. Consequently, we use image resolution 64×64 for GHI forecasting in this paper.

5.4. Generalization Ability Analysis

To rigorously position M3S-Net within the broader research landscape, we benchmarked its predictive performance against representative recent studies utilizing comparable public datasets (e.g., NREL SRRL) and forecast

Table 7

Comparison results of GHI with different methods on the SRRL dataset (%).

Model structure	Method	NRMSE (%)					
		10 MA	20 MA	30 MA	40 MA	50 MA	60 MA
Single-modal	LSTM	7.73	7.83	8.12	8.64	9.37	10.01
	DLinear	4.72	6.88	8.38	9.62	10.84	12.03
	TimesNet	5.12	6.39	7.29	8.15	8.99	9.84
	CNN-based	5.03	6.19	7.08	7.88	8.71	9.33
Multi-modal	ViT-based	5.04	6.16	7.02	7.92	8.66	9.36
	T2T	4.64	5.98	6.88	7.68	8.24	8.83
	M3S-Net	4.35	5.79	6.76	7.61	8.16	8.72

horizons. To ensure equitable comparison, the NRMSE was adopted as the unified evaluation metric. Table 7 summarizes the methodologies, forecast horizons, and reported NRMSE values for these related works. Ref. [58] employed a CNN backbone for feature extraction of series, reporting a 10-minute forecast NRMSE of 6.14%. While effective for spatial features, this approach lacks explicit temporal modeling of cloud dynamics.

Li et al. [25] converted the historical sequence into a 2D tensor using TimesNet and extracted temporal features using CNN, achieving NRMSE values between 4.64% and 6.88% for 10-to-30-minute horizons. In contrast, our proposed M3S-Net achieves a significantly lower NRMSE of 4.64% for 10-minute forecasts on comparable datasets. Furthermore, M3S-Net demonstrates superior or highly competitive performance across the entire 10-to-60-minute forecast range. This performance advantage is attributed to the synergistic integration of fine-grained cloud segmentation (MPCs-Net), comprehensive multi-scale temporal modeling (SIFR-Net), and the deep cross-modal fusion mechanism (MMIF) inherent to our architecture.

5.5. Model Interpretability and Visualization

To enhance model transparency and verify the physical meaningfulness of the learned features, we conducted a comprehensive visualization analysis of M3S-Net's key components. We utilized Gradient-weighted Class Activation Mapping (Grad-CAM) to generate heatmaps for the MPCs-Net module when processing typical multi-cloud images, as shown in Fig. 14. The heatmaps reveal that during fine-grained visual extraction branch, the model focuses its attention intensely on cloud regions actively moving toward or occluding the sun, specifically highlighting cloud edges and optically thick areas. This intuitive verification confirms that MPCs-Net successfully learns spatial features directly correlated with irradiance attenuation, rather than relying on spurious background correlations. By applying FFT to the input power sequence, we extracted dominant periodic components. Fig. 15 demonstrates that SIFR-Net successfully reshapes 1D time-series data into 2D tensor structures based on these dominant periods (e.g., diurnal cycles, short-term fluctuations). The module's scalable attention mechanism then learns intra-period variations and inter-period evolution

along the row and column dimensions, respectively, yielding physically meaningful feature representations. Finally, we extracted the interaction attention weights from the cross-modal Mamba layer in the MMIF module. Fig. 16 displays the weight heatmaps for visual and temporal features under sunny, cloudy, and overcast conditions. Under sunny conditions, the weights assigned to visual features are minimal, indicating that the model relies on the temporal regularity of the clear-sky curve. In contrast, under cloudy conditions, the visual weights become significantly more prominent, demonstrating the model's adaptability to visual data for predicting fluctuation trends. Weights in overcast remain consistently volatile, suggesting a continuous reliance on visual data to interpret complex, high-entropy sky conditions. These qualitative results confirm that the fusion module functions as a dynamic gate, modulating modal importance in response to real-time environmental contexts.

6. Conclusion

This study advances the domain of ultra-short-term PV power forecasting by transcending the inherent limitations of conventional binary cloud segmentation and shallow feature concatenation techniques. The proposed M3S-Net framework establishes a robust cross-modal semantic alignment between ground-based cloud imagery and meteorological time-series data. Specifically, by deploying the MPCN-Net to capture fine-grained cloud optical depth and the SIFR-Net to disentangle temporal periodicity, the framework effectively bridges the heterogeneous modality gap. Central to this innovation is the MMIF module, which incorporates a dynamic state-space matrix switching mechanism. This mechanism enables temporal contexts to adaptively modulate the representation of visual features. Extensive empirical evaluations conducted on the newly FGPD and NREL benchmark datasets substantiate the framework's performance, demonstrating significant improvements over existing SOTA baselines. However, acknowledging the framework's reliance on high-quality, fine-grained annotations, future investigations will prioritize semi-supervised or self-supervised domain adaptation techniques to enhance label efficiency and model generalization.

CRedit authorship contribution statement

Penghui Niu: Writing - original draft, Writing – review & editing, Visualization, Validation, Software, Methodology, Investigation, Funding acquisition. **Taotao Cai:** Writing – review & editing, Methodology, Investigation, Formal analysis. **Suqi Zhang:** Supervision, Resources, Project administration, Data curation. **Junhua Gu:** Supervision, Resources, Project administration, Funding acquisition, Data curation. **Ping Zhang:** Resources, Project administration, Funding acquisition. **Qiqi Liu:** Resources, Project administration, Investigation. **Jianxin Li:** Writing – review & editing, Supervision, Project administration, Methodology.

Declaration of competing interest

The authors declare that they have no known competing financial interests or personal relationships that could have appeared to influence the work reported in this paper.

Data availability

The proposed FGPD dataset and source code will be available at <https://github.com/she1110/FGPD>.

Acknowledgments

The research was supported by the National Natural Science Foundation of China under Grant No. 62206085, supported by the Innovation Capacity Improvement Plan Project of Hebei Province under 22567603H, and supported by the Interdisciplinary Postgraduate Training Program of Hebei University of Technology under HEBUT-Y-XKJC-2022101.

References

- [1] W. Lin, B. Zhang, H. Li, R. Lu, Multi-step prediction of photovoltaic power based on two-stage decomposition and bilstm, *Neurocomputing* 504 (2022) 56–67. doi:<https://doi.org/10.1016/j.neucom.2022.06.117>.
- [2] E. Kabir, P. Kumar, S. Kumar, A. A. Adelodun, K.-H. Kim, Solar energy: Potential and future prospects, *Renewable Sustainable Energy Rev.* 82 (2018) 894–900. doi:<https://doi.org/10.1016/j.rser.2017.09.094>.
- [3] V. A. Martinez Lopez, G. van Urk, P. J. Doodkorte, M. Zeman, O. Isabella, H. Ziar, Using sky-classification to improve the short-term prediction of irradiance with sky images and convolutional neural networks, *Sol. Energy* 269 (2024) 112320. doi:<https://doi.org/10.1016/j.solener.2024.112320>.
- [4] C. Zhang, L. Hua, C. Ji, M. Shahzad Nazir, T. Peng, An evolutionary robust solar radiation prediction model based on wt-ceemdan and iaso-optimized outlier robust extreme learning machine, *Appl. Energy* 322 (2022) 119518. doi:<https://doi.org/10.1016/j.apenergy.2022.119518>.
- [5] S. R. Sinsel, R. L. Riemke, V. H. Hoffmann, Challenges and solution technologies for the integration of variable renewable energy sources—a review, *Renewable Energy* 145 (2020) 2271–2285. doi:<https://doi.org/10.1016/j.renene.2019.06.147>.
- [6] C. Voyant, M. Muselli, C. Paoli, M.-L. Nivet, Numerical weather prediction (nwp) and hybrid arma/ann model to predict global radiation, *Energy* 39 (1) (2012) 341–355, *Sustainable Energy and Environmental Protection* 2010. doi:<https://doi.org/10.1016/j.energy.2012.01.006>.
- [7] B. Gao, X. Huang, J. Shi, Y. Tai, J. Zhang, Hourly forecasting of solar irradiance based on ceemdan and multi-strategy cnn-lstm neural networks, *Renewable Energy* 162 (2020) 1665–1683. doi:<https://doi.org/10.1016/j.renene.2020.09.141>.
- [8] C. Huang, L. Wang, L. L. Lai, Data-driven short-term solar irradiance forecasting based on information of neighboring sites, *IEEE Trans. Ind. Electron.* 66 (12) (2019) 9918–9927. doi:[10.1109/TIE.2018.2856199](https://doi.org/10.1109/TIE.2018.2856199).
- [9] P. Xia, L. Zhang, M. Min, J. Li, Y. Wang, Y. Yu, S. Jia, Accurate nowcasting of cloud cover at solar photovoltaic plants using geostationary satellite images, *Nat. Commun.* 15 (1) (JAN 13 2024). doi:[10.1038/s41467-023-44666-1](https://doi.org/10.1038/s41467-023-44666-1).
- [10] C. Shi, M. Zhang, H. Xiang, K. Zhang, S. Ju, X. Zhang, L. Han, A ground-based cloud image classification method for photovoltaic power prediction based on convolutional neural networks and vision transformer, *Eng. Appl. Artif. Intell.* 159 (2025) 111582. doi:<https://doi.org/10.1016/j.engappai.2025.111582>.

- [11] Y. Dai, W. Yu, M. Leng, A hybrid ensemble optimized bigru method for short-term photovoltaic generation forecasting, *Energy* 299 (2024) 131458. doi:<https://doi.org/10.1016/j.energy.2024.131458>.
- [12] J. Wang, Y. Yu, B. Zeng, H. Lu, Hybrid ultra-short-term pv power forecasting system for deterministic forecasting and uncertainty analysis, *Energy* 288 (2024) 129898. doi:<https://doi.org/10.1016/j.energy.2023.129898>.
- [13] S. Huang, Q. Zhou, J. Shen, H. Zhou, B. Yong, Multistage spatio-temporal attention network based on node for short-term pv power forecasting, *Energy* 290 (2024) 130308. doi:<https://doi.org/10.1016/j.energy.2024.130308>.
- [14] M. Trigo-González, M. Cortés-Carmona, A. Marzo, J. Alonso-Montesinos, M. Martínez-Durbán, G. López, C. Portillo, F. J. Batlles, Photovoltaic power electricity generation nowcasting combining sky camera images and learning supervised algorithms in the southern spain, *Renewable Energy* 206 (2023) 251–262. doi:<https://doi.org/10.1016/j.renene.2023.01.111>.
- [15] C. Feng, J. Zhang, W. Zhang, B.-M. Hodge, Convolutional neural networks for intra-hour solar forecasting based on sky image sequences, *Appl. Energy* 310 (2022) 118438. doi:<https://doi.org/10.1016/j.apenergy.2021.118438>.
- [16] A. H. Eşlik, E. Akarslan, F. O. Hocaoglu, Short-term solar radiation forecasting with a novel image processing-based deep learning approach, *Renewable Energy* 200 (2022) 1490–1505. doi:<https://doi.org/10.1016/j.renene.2022.10.063>.
- [17] J. Liu, H. Zang, T. Ding, L. Cheng, Z. Wei, G. Sun, Sky-image-derived deep decomposition for ultra-short-term photovoltaic power forecasting, *IEEE Trans. Sustainable Energy* 15 (2) (2024) 871–883. doi:<https://doi.org/10.1109/TSTE.2023.3312401>.
- [18] H. Zang, D. Chen, J. Liu, L. Cheng, G. Sun, Z. Wei, Improving ultra-short-term photovoltaic power forecasting using a novel sky-image-based framework considering spatial-temporal feature interaction, *Energy* 293 (2024) 130538. doi:<https://doi.org/10.1016/j.energy.2024.130538>.
- [19] W. Kong, Y. Jia, Z. Y. Dong, K. Meng, S. Chai, Hybrid approaches based on deep whole-sky-image learning to photovoltaic generation forecasting, *Appl. Energy* 280 (2020) 115875. doi:<https://doi.org/10.1016/j.apenergy.2020.115875>.
- [20] A. Dolatabadi, H. Abdeltawab, Y. A.-R. I. Mohamed, Deep reinforcement learning-based self-scheduling strategy for a caes-pv system using accurate sky images-based forecasting, *IEEE Trans. Power Syst.* 38 (2) (2023) 1608–1618. doi:<https://doi.org/10.1109/TPWRS.2022.3177704>.
- [21] G. Terrén-Serrano, M. Martínez-Ramón, Deep learning for intra-hour solar forecasting with fusion of features extracted from infrared sky images, *Inf. Fusion* 95 (2023) 42–61. doi:<https://doi.org/10.1016/j.inffus.2023.02.006>.
- [22] M. Caldas, R. Alonso-Suárez, Very short-term solar irradiance forecast using all-sky imaging and real-time irradiance measurements, *Renewable Energy* 143 (2019) 1643–1658. doi:<https://doi.org/10.1016/j.renene.2019.05.069>.
- [23] J. Liu, H. Zang, T. Ding, L. Cheng, Z. Wei, G. Sun, Harvesting spatiotemporal correlation from sky image sequence to improve ultra-short-term solar irradiance forecasting, *Renewable Energy* 209 (2023) 619–631. doi:<https://doi.org/10.1016/j.renene.2023.03.122>.
- [24] X. Wu, Z. Zhen, J. Zhang, F. Wang, F. Xu, H. Ren, Y. Su, Y. Sun, H. Yang, Multidimensional feature extraction based minutely solar irradiance forecasting method using all-sky images, *IEEE Trans. Ind. Appl.* 60 (3) (2024) 4494–4504. doi:<https://doi.org/10.1109/TIA.2024.3372515>.
- [25] H. Li, G. Ma, B. Wang, S. Wang, W. Li, Y. Meng, Multi-modal feature fusion model based on timesnet and t2t-vit for ultra-short-term solar irradiance forecasting, *Renewable Energy* 240 (2025) 122192. doi:<https://doi.org/10.1016/j.renene.2024.122192>.
- [26] W. Dou, K. Wang, S. Shan, M. Chen, K. Zhang, H. Wei, V. Sreeram, A multi-modal deep clustering method for day-ahead solar irradiance forecasting using ground-based cloud imagery and time series data, *Energy* 321 (2025) 135285. doi:<https://doi.org/10.1016/j.energy.2025.135285>.
- [27] J. Zhu, Y. Lin, C. Yang, K. Wang, Z. Zhang, Z. Zhao, L. Wang, Z. Lin, Q. Jin, C. Zheng, X. Wu, X. Gao, Hybrid modeling of direct normal irradiance for rooftop photovoltaic systems using multi-feature extraction from cloud images, *J. Build. Eng.* 106 (2025) 112571. doi:<https://doi.org/10.1016/j.jobte.2025.112571>.
- [28] X. Wei, D. Yue, G. P. Hancke, C. Dou, H. Li, Y. Qiu, Ultra short-term solar irradiance forecast based on multimodal data fusion and fuzzification, *IEEE Trans. Ind. Informatics* 21 (4) (2025) 3256–3265. doi:<https://doi.org/10.1109/TII.2024.3523575>.
- [29] B. Nie, Z. Lu, J. Han, W. Chen, C. Cai, W. Pan, Investigation on ground-based cloud image classification and its application in photovoltaic power forecasting, *IEEE Trans. Instrum. Meas.* 74 (2025) 1–11. doi:<https://doi.org/10.1109/TIM.2025.3529074>.
- [30] Y. Ma, W. Yu, J. Zhu, Z. You, A. Jia, Research on ultra-short-term photovoltaic power forecasting using multimodal data and ensemble learning, *Energy* 330 (2025) 136831. doi:<https://doi.org/10.1016/j.energy.2025.136831>.
- [31] X. Wei, X. Wu, K. Yoshimura, C. Cheng, H. Huang, Z. Ding, Y. Song, Climate-informed long-term forecasting of wind and photovoltaic power using a hybrid dwt-bes-cnn-lstm model, *Energy* 338 (2025) 138677. doi:<https://doi.org/10.1016/j.energy.2025.138677>.
- [32] Y. Xiang, Y. Yang, L. Xu, Z. Tang, Y. Liu, W. Sun, J. Liu, A dynamic meteorological correlation integrated hybrid method for photovoltaic output forecasting, *Renewable Energy* 256 (2026) 124561. doi:<https://doi.org/10.1016/j.renene.2025.124561>.
- [33] C. Shi, M. Zhang, H. Xiang, K. Zhang, S. Ju, X. Zhang, L. Han, A ground-based cloud image classification method for photovoltaic power prediction based on convolutional neural networks and vision transformer, *Eng. Appl. Artif. Intell.* 159 (2025) 111582. doi:<https://doi.org/10.1016/j.engappai.2025.111582>.
- [34] B. Yong, Y. Zhang, J. Shen, A. Ren, X. Zhou, Q. Zhou, Convodemixer: A multimodal deep learning model for ultra-short-term pv power forecasting, *Sol. Energy* 300 (2025) 113777. doi:<https://doi.org/10.1016/j.solener.2025.113777>.
- [35] Z. Su, C. Shi, K. Zhang, X. Xie, X. Zhang, J. Xiao, Transcloudnet: a dual-branch feature fusion ground-based cloud image fine-grained segmentation method for photovoltaic power prediction, *Energy Convers. Manage.* 348 (2026) 120647. doi:<https://doi.org/10.1016/j.enconman.2025.120647>.
- [36] T. Stoffel, A. Andreas, Nrel solar radiation research laboratory (srri): Baseline measurement system (bms); golden, colorado (data), Tech. rep., National Renewable Energy Lab.(NREL), Golden, CO (United States) (1981). doi:<http://dx.doi.org/10.7799/1052221>.
- [37] H. T. C. Pedro, D. P. Larson, C. F. M. Coimbra, A comprehensive dataset for the accelerated development and benchmarking of solar forecasting methods, *J. Renewable Sustainable Energy* 11 (3) (2019) 036102. doi:<https://doi.org/10.1063/1.5094494>.
- [38] M. Haeffelin, L. Barthès, O. Bock, C. Boitel, S. Bony, D. Bouniol, H. Chepfer, M. Chiriaco, J. Cuesta, J. Delanoë, P. Drobinski, J.-L. Dufresne, C. Flamant, M. Grall, A. Hodzic, F. Hourdin, F. Lapouge, Y. Lemaître, A. Mathieu, Y. Morille, C. Naud, V. Noël, W. O'Hirok, J. Pelon, C. Pietras, A. Protat, B. Romand, G. Scialom, R. Vautard, Sirta, a ground-based atmospheric observatory for cloud and aerosol research, *Ann. Geophys.* 23 (2) (2005) 253–275. doi:<https://doi.org/10.5194/angeo-23-253-2005>.
- [39] W. Xie, D. Liu, M. Yang, S. Chen, B. Wang, Z. Wang, Y. Xia, Y. Liu, Y. Wang, C. Zhang, Segcloud: a novel cloud image segmentation model using a deep convolutional neural network for ground-based all-sky-view camera observation, *Atmos. Meas. Tech.* 13 (4) (2020) 1953–1961. doi:<https://doi.org/10.5194/amt-13-1953-2020>.
- [40] S. Dev, F. M. Savoy, Y. H. Lee, S. Winkler, WAHRIS: A low-cost high-resolution whole sky imager with near-infrared capabilities, in: G. C. Holst, K. A. Krapels, G. H. Ballard, J. A. B. Jr., R. L. M. Jr. (Eds.), *Infrared Imaging Systems: Design, Analysis, Modeling, and Testing XXV*, Vol. 9071, International Society for Optics and Photonics, SPIE, 2014, p. 90711L. doi:<https://doi.org/10.1117/12.2052982>.
- [41] P. Niu, J. She, T. Cai, Y. Zhang, P. Zhang, J. Gu, J. Li, Mpcm-net: A multi-scale network that integrates partial attention convolution with

- mamba for ground-based cloud image segmentation, *IEEE Trans. Geosci. Remote. Sens.* (2026) 1–1 [doi:10.1109/TGRS.2026.3666092](https://doi.org/10.1109/TGRS.2026.3666092).
- [42] J. Hu, L. Shen, S. Albanie, G. Sun, E. Wu, Squeeze-and-excitation networks, *IEEE Trans. Pattern Anal. Mach. Intell.* 42 (8) (2020) 2011–2023. [doi:10.1109/TPAMI.2019.2913372](https://doi.org/10.1109/TPAMI.2019.2913372).
- [43] P. Niu, T. Cai, J. She, Y. Zhang, J. Gua, P. Zhanga, J. Hane, J. Li, Usf-net: A unified spatiotemporal fusion network for ground-based remote sensing cloud image sequence extrapolation, *arXiv preprint arXiv:2511.09045* (2025). [doi:https://doi.org/10.48550/arXiv.2511.09045](https://doi.org/10.48550/arXiv.2511.09045).
- [44] A. Dosovitskiy, L. Beyer, A. Kolesnikov, D. Weissenborn, X. Zhai, T. Unterthiner, M. Dehghani, M. Minderer, G. Heigold, S. Gelly, J. Uszkoreit, N. Houlsby, **An image is worth 16x16 words: Transformers for image recognition at scale**, in: *Proc. Int. Conf. Learn. Represent. (ICLR)*, Virtual Event, Austria, 2021, pp. 3–7. URL <https://openreview.net/forum?id=YicbFdNTTy>
- [45] J. Zhang, Y. Zhang, J. Gu, Y. Zhang, L. Kong, X. Yuan, **Accurate image restoration with attention retractable transformer**, in: *Int. Conf. Learn. Represent. (ICLR)*, Kigali, Rwanda, 2023. URL <https://openreview.net/forum?id=IloMJ5rqfnt>
- [46] Z. Liu, Y. Lin, Y. Cao, H. Hu, Y. Wei, Z. Zhang, S. Lin, B. Guo, Swin transformer: Hierarchical vision transformer using shifted windows, in: *Proc. IEEE Int. Conf. Comput. Vision. (ICCV)*, Montreal, QC, Canada, 2021, pp. 9992–10002. [doi:10.1109/ICCV48922.2021.00986](https://doi.org/10.1109/ICCV48922.2021.00986).
- [47] S. Wang, J. Li, X. Shi, Z. Ye, B. Mo, W. Lin, S. Ju, Z. Chu, M. Jin, **Timemixer++: A general time series pattern machine for universal predictive analysis**, in: *Int. Conf. Learn. Represent. (ICLR)*, Singapore, 2025. URL <https://openreview.net/forum?id=1CLzLXSFNn>
- [48] Y. Liu, Y. Tian, Y. Zhao, H. Yu, L. Xie, Y. Wang, Q. Ye, J. Jiao, Y. Liu, **Vmamba: Visual state space model**, in: *Proc. Adv. neural inf. proces. syst. (NIPS)*, Vancouver, BC, Canada, 2024, pp. 103031–103063. URL http://papers.nips.cc/paper_files/paper/2024/hash/baa2da9ae4bfed26520bb61d259a3653-Abstract-Conference.html
- [49] Z. Wan, P. Zhang, Y. Wang, S. Yong, S. Stepputtis, K. P. Sycara, Y. Xie, Sigma: Siamese mamba network for multi-modal semantic segmentation, in: *Proc. IEEE Winter Conf. Appl. Comput. Vis. (WACV)*, Tucson, AZ, USA, 2025, pp. 1734–1744. [doi:10.1109/WACV61041.2025.00176](https://doi.org/10.1109/WACV61041.2025.00176).
- [50] X. Hu, Y. Tai, X. Zhao, C. Zhao, Z. Zhang, J. Li, B. Zhong, J. Yang, Exploiting multimodal spatial-temporal patterns for video object tracking, in: *Proc. AAAI Conf. Artif. Intell. (AAAI)*, Philadelphia, PA, USA, 2025, pp. 3581–3589. [doi:10.1609/AAAI.V39I4.32372](https://doi.org/10.1609/AAAI.V39I4.32372).
- [51] O. Ronneberger, P. Fischer, T. Brox, U-net: Convolutional networks for biomedical image segmentation, in: *Proc. Int. Conf. Med. Image Comput. Comput.-Assist. Intervent. (MICCAI)*, Munich, Germany, 2015, pp. 234–241. [doi:10.1007/978-3-319-24574-4_28](https://doi.org/10.1007/978-3-319-24574-4_28).
- [52] C. Shi, Z. Su, K. Zhang, X. Xie, X. Zheng, Q. Lu, J. Yang, Cloudfunet: A fine-grained segmentation method for ground-based cloud images based on an improved encoder-decoder structure, *IEEE Trans. Geosci. Remote. Sens.* 62 (2024) 1–13. [doi:10.1109/TGRS.2024.3389089](https://doi.org/10.1109/TGRS.2024.3389089).
- [53] E. Xie, W. Wang, Z. Yu, A. Anandkumar, J. M. Álvarez, P. Luo, **Segformer: Simple and efficient design for semantic segmentation with transformers**, in: *Proc. Adv. neural inf. proces. syst. (NIPS)*, Virtual, Online, 2021, pp. 12077–12090. URL <https://proceedings.neurips.cc/paper/2021/hash/64f1f27bf1b4ec22924fd0acb550c235-Abstract.html>
- [54] C. Shi, Z. Su, K. Zhang, X. Xie, X. Zhang, Cloudswinnet: A hybrid cnn-transformer framework for ground-based cloud images fine-grained segmentation, *Energy* 309 (2024) 133128. [doi:https://doi.org/10.1016/j.energy.2024.133128](https://doi.org/10.1016/j.energy.2024.133128).
- [55] S. Hochreiter, J. Schmidhuber, Long short-term memory, *Neural Comput.* 9 (8) (1997) 1735–1780. [doi:10.1162/neco.1997.9.8.1735](https://doi.org/10.1162/neco.1997.9.8.1735).
- [56] A. Zeng, M. Chen, L. Zhang, Q. Xu, Are transformers effective for time series forecasting?, in: *Proc. AAAI Conf. Artif. Intell. (AAAI)*, Washington, DC, USA, 2023, pp. 11121–11128. [doi:10.1609/AAAI.V37I9.26317](https://doi.org/10.1609/AAAI.V37I9.26317).
- [57] H. Wu, T. Hu, Y. Liu, H. Zhou, J. Wang, M. Long, Timesnet: Temporal 2d-variation modeling for general time series analysis, *arXiv preprint arXiv:2210.02186* (2022). [doi:https://doi.org/10.48550/arXiv.2210.02186](https://doi.org/10.48550/arXiv.2210.02186).
- [58] C. Feng, J. Zhang, W. Zhang, B.-M. Hodge, Convolutional neural networks for intra-hour solar forecasting based on sky image sequences, *Appl. Energy* 310 (2022) 118438. [doi:https://doi.org/10.1016/j.apenergy.2021.118438](https://doi.org/10.1016/j.apenergy.2021.118438).
- [59] J. Liu, H. Zang, L. Cheng, T. Ding, Z. Wei, G. Sun, A transformer-based multimodal-learning framework using sky images for ultra-short-term solar irradiance forecasting, *Appl. Energy* 342 (2023) 121160. [doi:https://doi.org/10.1016/j.apenergy.2023.121160](https://doi.org/10.1016/j.apenergy.2023.121160).

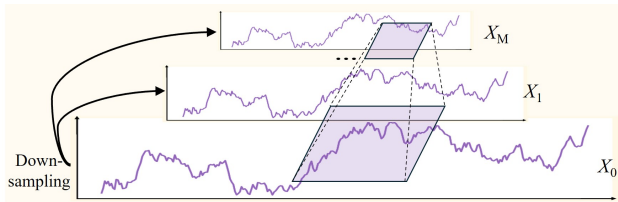


Fig. 4: The flowchart of the multi-scale representation.

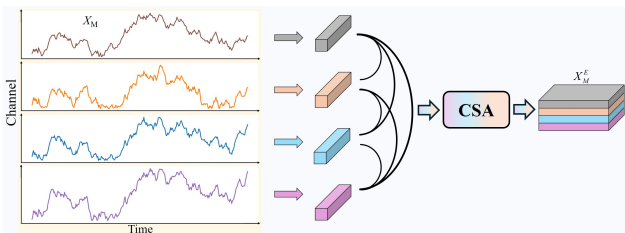


Fig. 5: The flowchart of the CSA to capture nonlinear interdependencies among variables on the coarsest scale X_M .

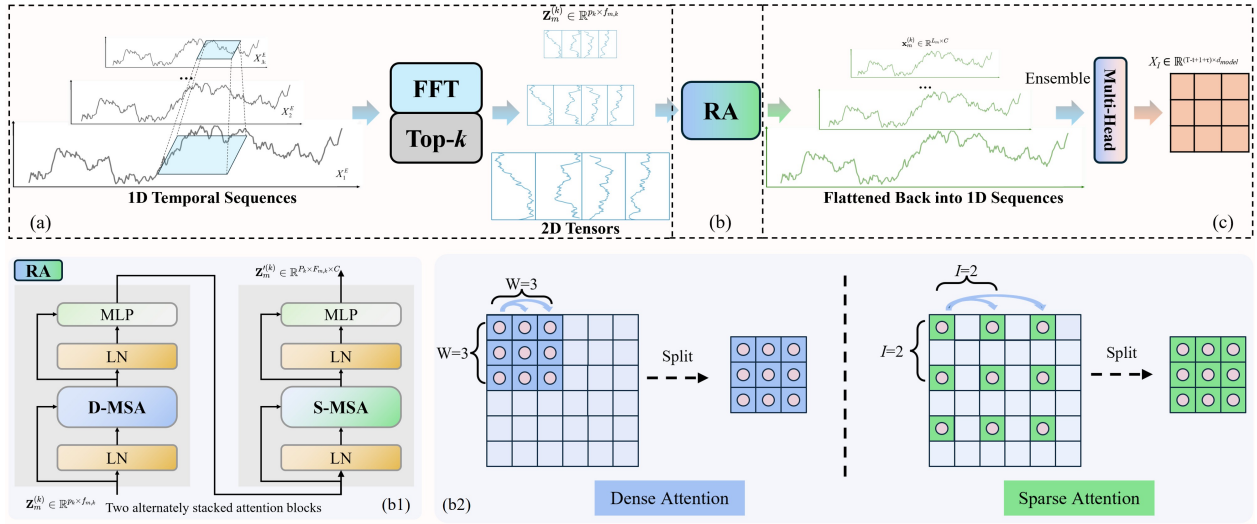


Fig. 6: The flowchart of (a) FFT-based 2D transformation. (b) RA. (c) Amplitude-weighted fusion and prediction. The architecture of (b1) RA, (b2) D-MSA and S-MSA.

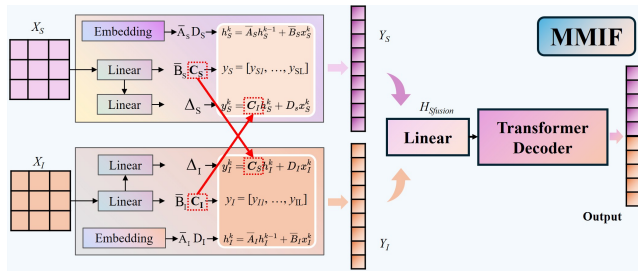


Fig. 7: The architecture of the proposed MMIF.

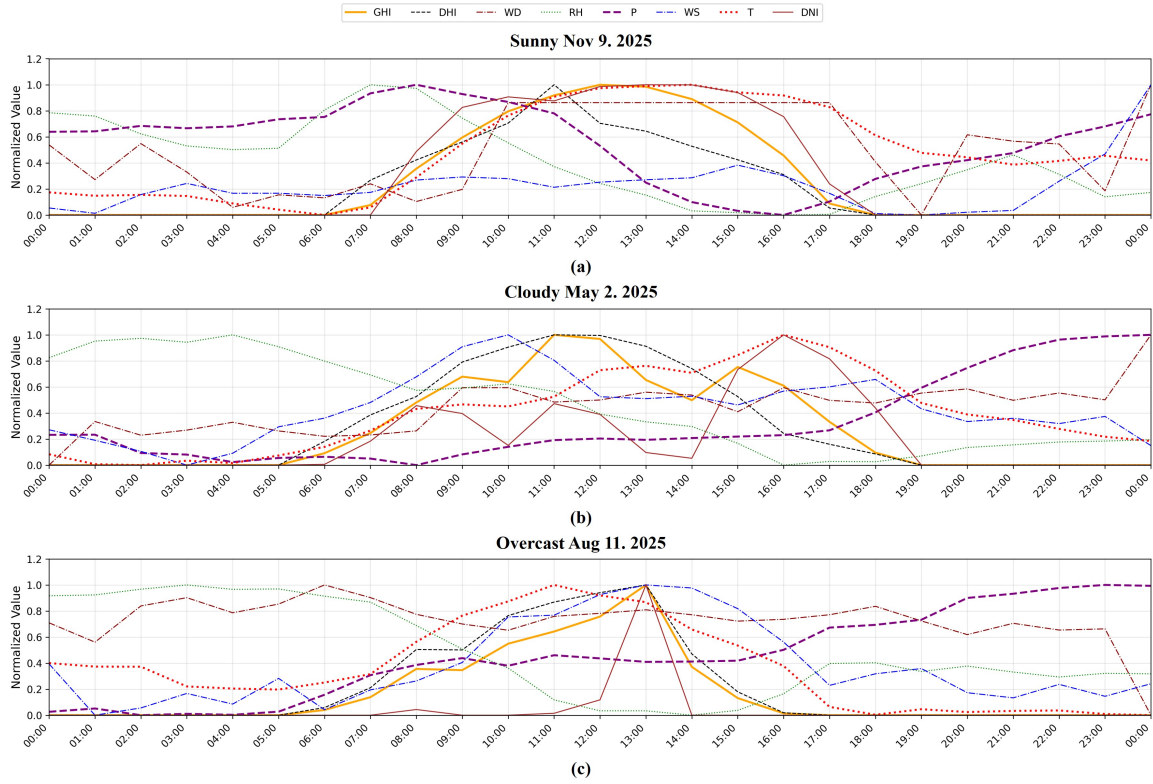


Fig. 8: Eight types of meteorological data under three types of typical weather.

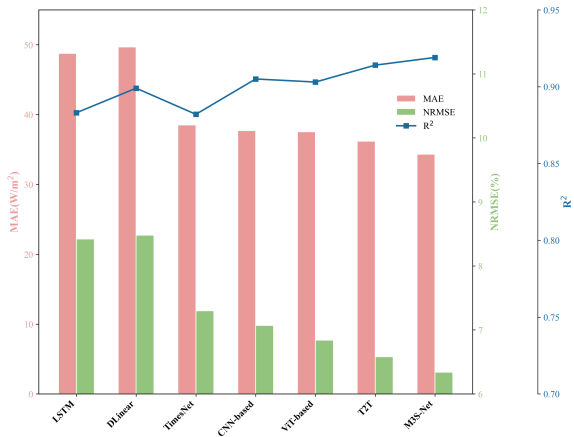


Fig. 9: Visual results of average value of different error indicators.

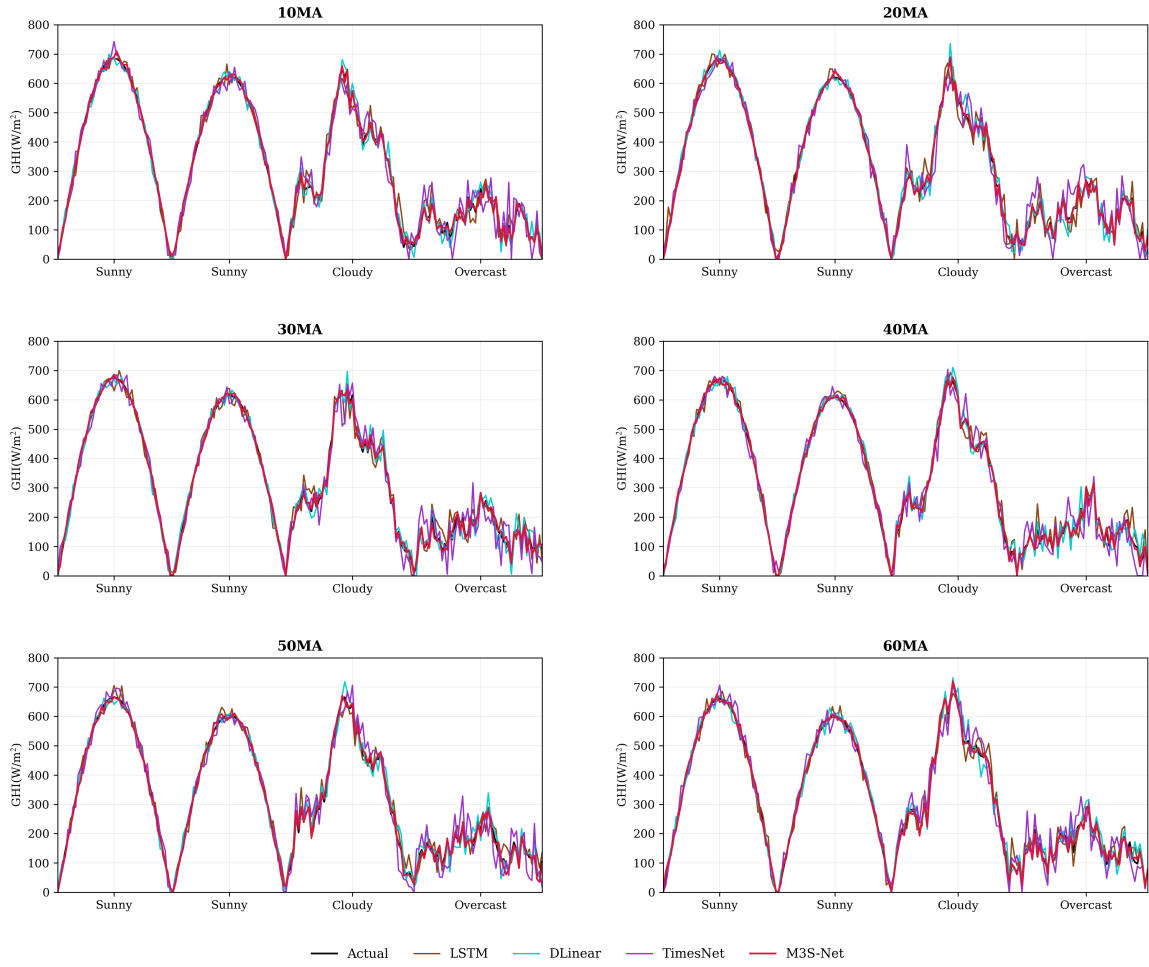


Fig. 10: Visual results under three typical weather categories of the proposed M3S-Net and other singlemodal methods.

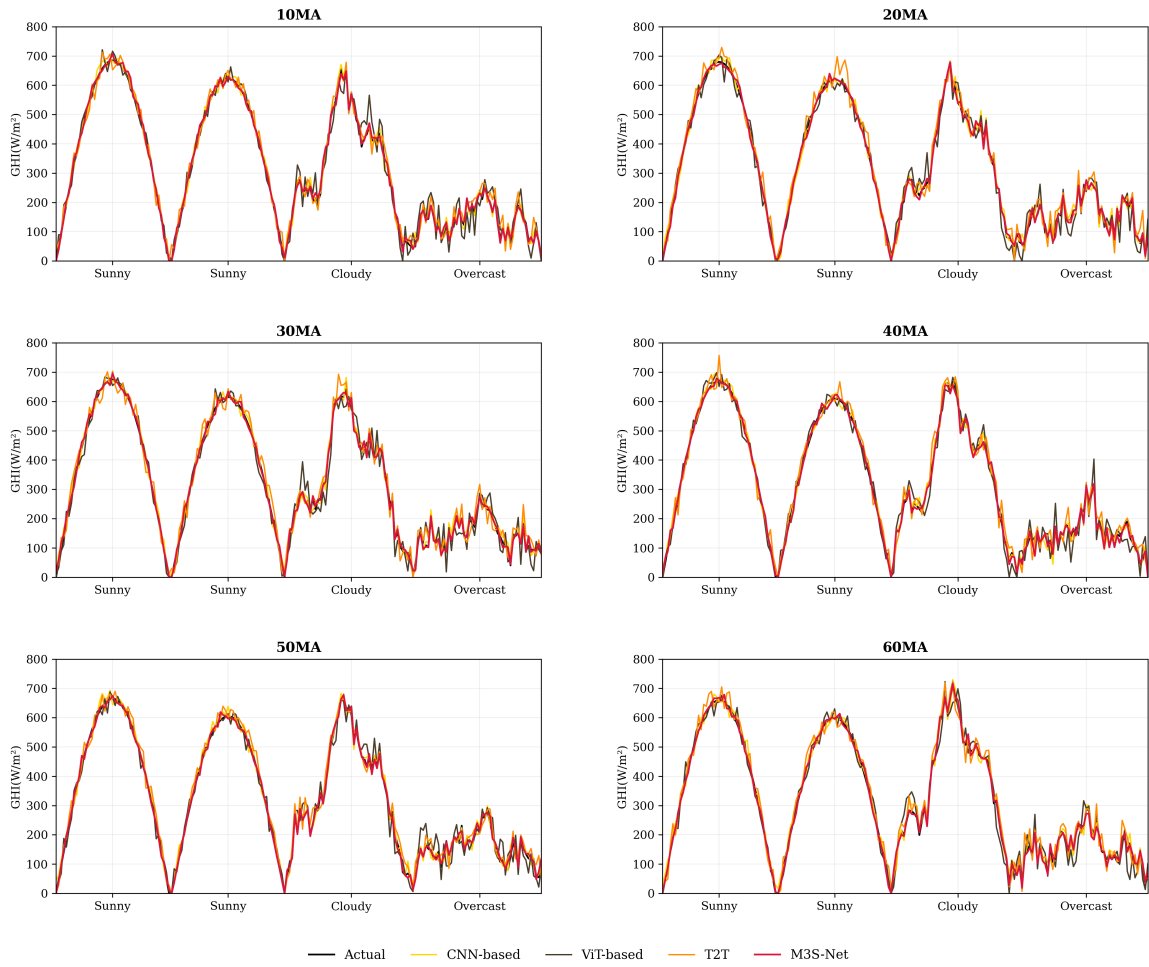


Fig. 11: Visual results under three typical weather categories of the proposed M3S-Net and other multimodal methods.

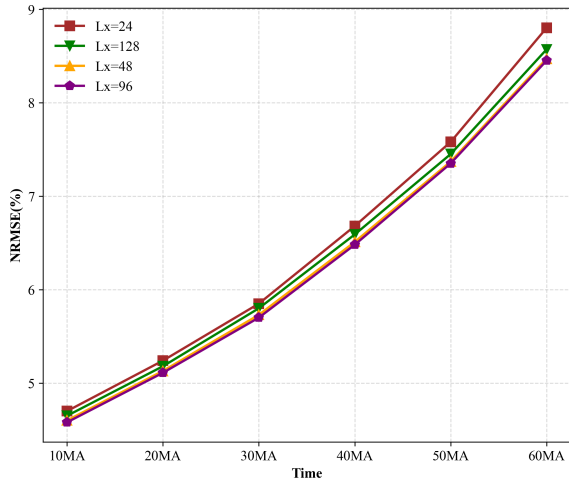


Fig. 12: Visualization of the impact of input lengths in SIFR-Net.

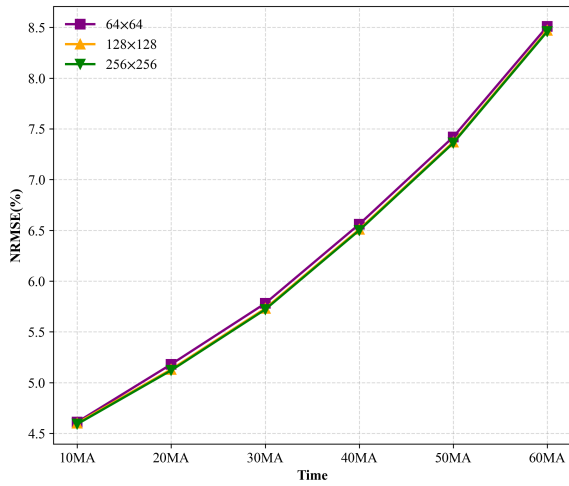


Fig. 13: Visualization of the impact of image resolution in MPCS-Net.

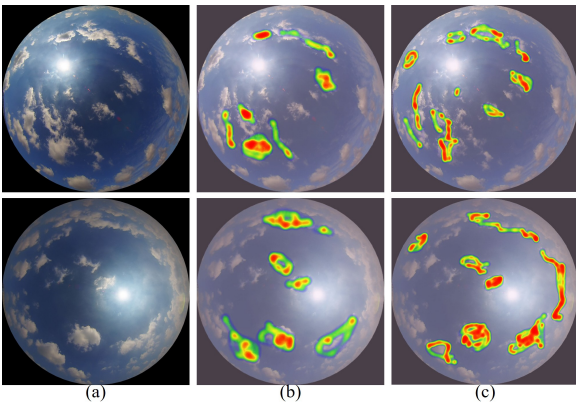


Fig. 14: Visualization results show different categories of the FGPD validation set using Grad-CAM. (a) Input image, (b) MPCM-Net, and (c) MPCS-Net.

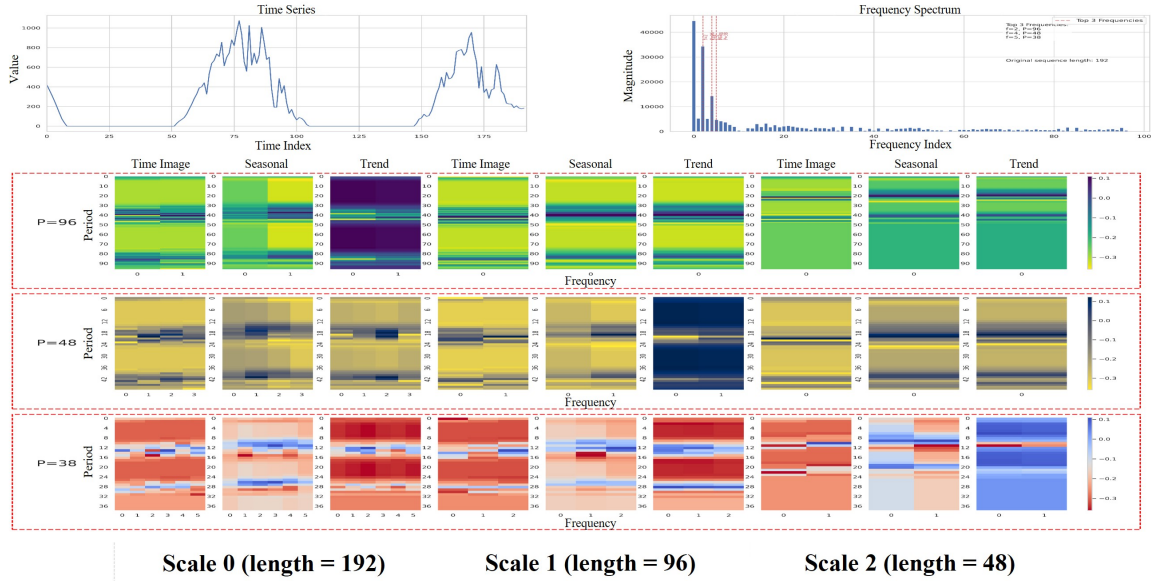


Fig. 15: Visualization of representation on FGPD across three different scales (length: 192, 96, 48) and three periods (96, 48, 36) with frequencies (2, 4, 5). Both high-frequency local fluctuations and low-frequency seasonal trends via spectral-temporal disentanglement are captured.

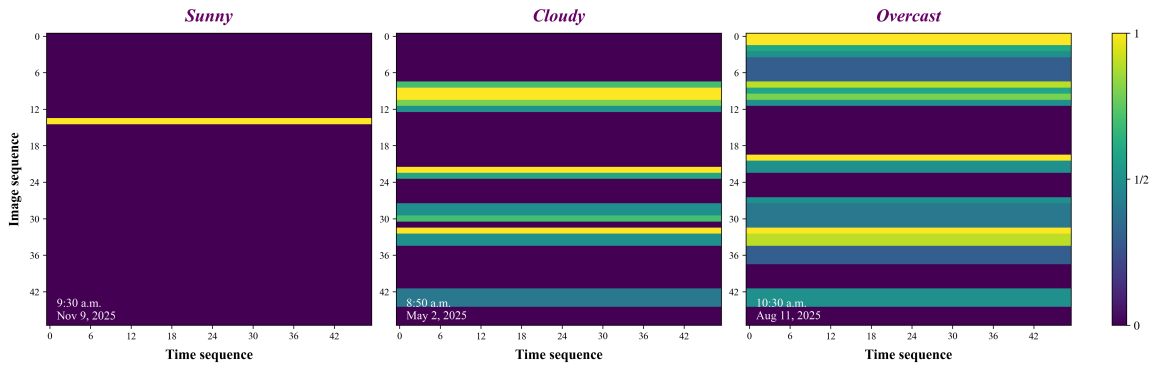


Fig. 16: The heatmaps of visual and temporal weights of MMIF under different weather conditions. Highlight performance along the horizontal axis indicates the difference in the visual feature activation. Visual feature is activated to enhance temporal features to participate in GHI forecasting.